Table 2 Spinal blood flow (SBF)

Cervical	*12 W*		*16 W*		*19 W*	
	WT	*Tg*	*WT*	*Tg*	*WT*	*Tg*
GM						
AH (R)	96.7 ± 12.5	78.0 ± 13.6*	104.3 ± 19.5	64.0 ± 8.7**	104.9 ± 13.4	49.8 ± 5.5**
AH (L)	99.3 ± 12.5	79.8 ± 5.4*	106.0 ± 18.3	64.7 ± 15.9**	107.2 ± 9.4	51.6 ± 5.7**
MH	91.2 ± 10.5	82.3 ± 7.1	99.5 ± 18.4	65.3 ± 13.3**	105.8 ± 14.3	50.1 ± 5.0**
DH (R)	83.5 ± 8.4	69.8 ± 9.9*	82.5 ± 9.5	62.9 ± 11.7*	90.0 ± 3.4	44.9 ± 3.8**
DH (L)	82.4 ± 11.0	71.1 ± 3.3*	81.4 ± 12.5	63.6 ± 15.2	88.0 ± 8.6	48.4 ± 6.4**
WM						
AF	46.5 ± 9.3	53.5 ± 2.9	47.1 ± 6.3	48.9 ± 6.0	43.9 ± 8.0	40.6 ± 2.0
LF (R)	48.0 ± 8.3	48.9 ± 6.5	45.9 ± 7.1	46.2 ± 2.9	46.1 ± 10.3	37.4 ± 3.0
LF (L)	47.4 ± 4.8	54.6 ± 6.6	46.5 ± 7.1	50.9 ± 9.8	50.4 ± 8.6	38.1 ± 5.0*
DF	45.6 ± 6.6	45.4 ± 3.2	46.4 ± 5.8	47.2 ± 7.8	44.2 ± 8.8	35.9 ± 6.0
Thoracic	*12 W*		*16 W*		*19 W*	
	WT	*Tg*	*WT*	*Tg*	*WT*	*Tg*
GM						
AH (R)	79.4 ± 9.4	67.6 ± 6.2*	88.1 ± 1.9	59.9 ± 9.4**	80.7 ± 6.7	46.9 ± 4.7**
AH (L)	79.0 ± 11.3	66.0 ± 2.7*	85.8 ± 3.7	58.4 ± 10.0**	79.8 ± 7.3	47.1 ± 5.5**
MH	77.5 ± 9.4	67.0 ± 3.7*	78.5 ± 2.2	56.6 ± 5.2**	75.0 ± 10.5	45.4 ± 5.2**
DH (R)	68.2 ± 8.1	60.5 ± 6.7	68.4 ± 1.8	56.5 ± 8.5*	66.0 ± 3.8	44.3 ± 5.5**
DH (L)	68.2 ± 12.4	62.2 ± 2.7	66.8 ± 3.0	52.2 ± 4.0**	71.7 ± 9.1	45.3 ± 7.9**
WM						
AF	47.7 ± 4.0	47.9 ± 5.8	45.1 ± 1.7	46.8 ± 9.5	43.9 ± 8.9	37.7 ± 3.8
LF (R)	43.2 ± 5.3	43.7 ± 5.8	43.4 ± 1.3	42.2 ± 5.3	42.5 ± 8.9	37.7 ± 5.5
LF (L)	39.7 ± 4.8	46.1 ± 5.8	44.6 ± 1.9	38.9 ± 3.6	43.8 ± 8.6	35.6 ± 6.4
DF	44.6 ± 3.7	46.2 ± 4.7	43.1 ± 2.0	47.8 ± 8.4	43.0 ± 6.9	38.5 ± 6.5
Lumbar	*12 W*		*16 W*		*19 W*	
	WT	*Tg*	*WT*	*Tg*	*WT*	*Tg*
GM						
AH (R)	103.1 ± 14.1	74.3 ± 14.0**	119.9 ± 20.8	62.4 ± 7.3**	116.1 ± 22.3	49.0 ± 5.6**
AH (L)	103.0 ± 4.6	81.9 ± 9.1**	115.3 ± 19.8	66.3 ± 14.3**	114.2 ± 20.7	51.4 ± 7.7**
MH	104.0 ± 11.7	80.8 ± 7.9**	112.5 ± 24.1	60.7 ± 8.0**	120.2 ± 50.8	49.2 ± 6.9*
DH (R)	88.7 ± 13.7	67.7 ± 10.3*	87.0 ± 11.3	58.3 ± 5.4**	96.0 ± 10.2	45.8 ± 3.8**
DH (L)	86.9 ± 10.5	76.5 ± 8.7	85.6 ± 10.3	58.4 ± 8.2**	96.4 ± 9.6	50.5 ± 7.7**
WM						
AF	50.2 ± 4.2	51.1 ± 4.3	48.6 ± 5.9	50.3 ± 6.5	50.8 ± 4.5	40.9 ± 4.6*
LF (R)	45.8 ± 6.7	47.4 ± 3.7	46.4 ± 6.6	45.6 ± 5.8	45.9 ± 10.1	39.3 ± 3.6
LF (L)	49.7 ± 7.9	54.9 ± 8.4	45.4 ± 7.3	46.7 ± 4.1	54.8 ± 7.2	38.6 ± 3.8**
DF	47.6 ± 4.2	50.2 ± 4.4	46.1 ± 5.1	46.2 ± 8.2	48.7 ± 4.4	40.4 ± 3.8*

AF, anterior funiculus; AH, anterior horn; DF, dorsal funiculus; DH, dorsal horn; GM, gray matter; LF, lateral funiculus; MH, middle region of AH; Tg, transgenic; WM, white matter; WT, wild type.
The values are expressed as mean values ± s.d.
*$P < 0.05$, **$P < 0.01$ versus age-matched WT mice.

Figure 3 Regional spinal blood flow (SBF) in anterior horn (AH), dorsal horn (DH), anterior and dorsal funiculus (AF + DF), and lateral funiculus (LF) of cervical (**A–C**), thoracic (**D–F**), and lumber cord (**G–I**) of 12, 16, and 19 W in wild-type (WT) ($n = 5$ at each W) and transgenic (Tg) mice ($n = 6, 5, 5$ at each W). Local spinal glucose utilization (LSGU) in AH, DH, AF + DF, and LF of cervical (**J–L**), thoracic (**M–O**), and lumber cord (**P–R**) of 12, 16, and 19 W in WT ($n = 5$ at each W) and Tg mice ($n = 6, 5, 5$ at each W). LSGU/SBF ratio in AH, DH, AF + DF, and LF of cervical (**S–U**), thoracic (**V–X**), and lumber cord (**Y–AA**) of 12, 16, and 19 W in WT and Tg mice. *$P < 0.05$, **$P < 0.01$ versus age-matched WT mice.

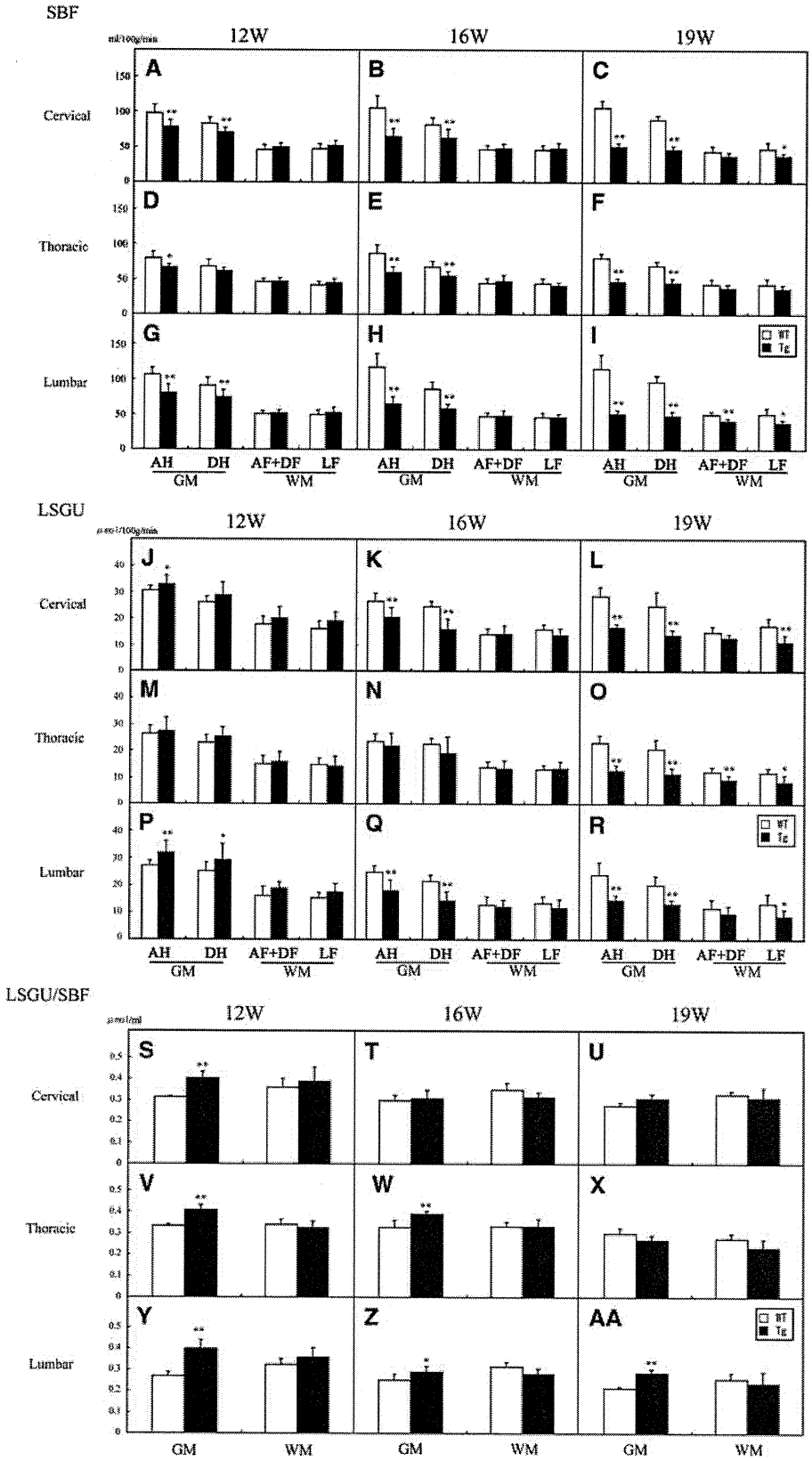
SBF
12W
16W
19W
Cervical
Thoracic
Lumbar
A
B
C
D
E
F
G
H
I
WT
Tg
AH
DH
AF+DF
LF
GM
WM
LSGU
J
K
L
M
N
O
P
Q
R
LSGU/SBF
S
T
U
V
W
X
Y
Z
AA

Table 3 Local spinal glucose utilization (LSGU)

Cervical	*12 W*		*16 W*		*19 W*	
	WT	*Tg*	*WT*	*Tg*	*WT*	*Tg*
GM						
AH (R)	30.9 ± 1.8	33.6 ± 3.6**	26.1 ± 3.1	20.0 ± 4.5*	27.1 ± 1.2	16.3 ± 1.0**
AH (L)	30.2 ± 1.7	32.1 ± 3.4	26.9 ± 3.6	20.9 ± 3.3*	30.1 ± 4.3	16.9 ± 2.0**
MH	28.5 ± 4.1	30.9 ± 4.3	26.2 ± 2.5	18.4 ± 4.1**	29.6 ± 5.7	15.6 ± 3.2**
DH (R)	26.3 ± 2.4	30.3 ± 3.7*	24.3 ± 2.3	16.2 ± 4.4**	23.3 ± 2.6	13.6 ± 1.7**
DH (L)	26.0 ± 2.3	27.0 ± 5.9	24.6 ± 2.3	15.5 ± 4.1**	26.0 ± 7.8	13.5 ± 2.8*
WM						
AF	16.8 ± 2.8	19.3 ± 3.6	14.8 ± 1.6	14.8 ± 3.9	14.6 ± 2.4	13.4 ± 1.5
LF (R)	17.4 ± 3.7	21.0 ± 2.7	16.4 ± 1.4	14.1 ± 3.2	16.1 ± 2.1	12.9 ± 2.1*
LF (L)	14.7 ± 1.5	17.0 ± 3.0	15.2 ± 2.6	13.4 ± 1.7	18.4 ± 3.4	9.4 ± 2.2**
DF	18.7 ± 3.1	20.7 ± 5.3	13.3 ± 2.8	13.5 ± 2.1	15.0 ± 2.3	11.8 ± 1.5*
Thoracic	*12 W*		*16 W*		*19 W*	
	WT	*Tg*	*WT*	*Tg*	*WT*	*Tg*
GM						
AH (R)	25.9 ± 3.8	26.2 ± 5.4	23.1 ± 1.9	22.5 ± 4.9	21.1 ± 1.2	12.0 ± 2.4**
AH (L)	26.8 ± 2.0	28.5 ± 5.1	23.8 ± 3.7	20.6 ± 5.5	24.8 ± 2.9	13.3 ± 1.3**
MH	25.3 ± 1.8	27.6 ± 4.5	23.6 ± 2.2	20.4 ± 4.8	24.4 ± 6.6	13.8 ± 2.8*
DH (R)	23.8 ± 3.9	25.9 ± 3.6	21.8 ± 1.8	19.3 ± 5.2	18.4 ± 1.6	11.7 ± 2.0**
DH (L)	22.2 ± 1.1	24.4 ± 4.3	22.8 ± 3.0	18.9 ± 7.4	23.0 ± 3.3	11.2 ± 2.7**
WM						
AF	15.8 ± 2.8	16.1 ± 2.9	15.2 ± 1.7	14.2 ± 3.1	13.5 ± 0.1	9.6 ± 2.3*
LF (R)	15.0 ± 3.1	16.1 ± 3.5	12.8 ± 1.3	13.2 ± 2.3	11.5 ± 1.2	10.1 ± 1.9
LF (L)	14.6 ± 1.7	12.3 ± 3.4	13.3 ± 1.9	13.2 ± 3.7	12.1 ± 2.4	6.4 ± 2.7*
DF	14.2 ± 4.0	15.5 ± 4.7	12.6 ± 2.0	12.5 ± 3.2	10.9 ± 1.9	8.7 ± 1.3
Lumbar	*12 W*		*16 W*		*19 W*	
	WT	*Tg*	*WT*	*Tg*	*WT*	*Tg*
GM						
AH (R)	27.8 ± 2.2	33.1 ± 3.6**	24.6 ± 2.3	19.0 ± 4.2*	23.8 ± 1.4	14.1 ± 2.3**
AH (L)	26.3 ± 1.4	30.5 ± 5.0*	26.5 ± 2.4	17.9 ± 4.7**	25.2 ± 7.0	15.6 ± 1.5*
MH	25.8 ± 1.7	29.1 ± 5.4	23.9 ± 1.9	15.8 ± 4.2**	24.8 ± 3.8	13.0 ± 2.7**
DH (R)	23.9 ± 4.0	30.0 ± 5.3*	21.9 ± 2.4	15.6 ± 2.8**	20.5 ± 2.3	13.8 ± 1.3**
DH (L)	26.3 ± 1.9	28.6 ± 6.8	22.3 ± 2.8	13.7 ± 4.2**	20.9 ± 4.9	13.2 ± 2.0*
WM						
AF	17.0 ± 2.6	19.5 ± 2.4	14.2 ± 1.9	13.1 ± 3.0	12.8 ± 2.6	11.9 ± 0.7
LF (R)	16.1 ± 2.2	18.9 ± 3.3	14.1 ± 3.0	13.1 ± 3.8	13.5 ± 3.5	10.9 ± 1.5
LF (L)	14.4 ± 1.8	16.2 ± 2.5	13.6 ± 2.4	10.8 ± 2.8	13.9 ± 4.6	6.8 ± 1.8*
DF	15.2 ± 3.9	18.0 ± 2.2	11.8 ± 4.1	11.6 ± 2.7	11.1 ± 3.9	8.1 ± 3.1

AF, anterior funiculus; AH, anterior horn; DF, dorsal funiculus; DH, dorsal horn; GM, gray matter; LF, lateral funiculus; MH, middle region of AH; Tg, transgenic; WM, white matter; WT, wild type.
The values are expressed as mean ± s.d.
*$P < 0.05$, **$P < 0.01$ versus age-matched WT mice.

Discussion

In the present study, we first performed an *in vivo* capillary imaging of lumbar spinal cord using two-photon microscope. In Tg mice, capillary diameter in AH of lumbar cord became progressively smaller (Figures 1A–1F), capillary density became lower (Figure 1G), and mean RBC speed progressively decreased during the disease course (Figures 1H–1L), resulting in progressive decrease of flow volume only in Tg mice (Figure 1M). We then analyzed SBF and LSGU of cervical, thoracic, and lumbar cord using standard autoradiographic technique. In Tg mice, SBF was significantly decreased in GM, especially AH, before motor neuron loss at 12 W, and then progressively decreased with disease progression from 16 to 19 W (Table 2; Figures 2E–2P and Figures 3A–3I). Contrary to the results of SBF,

Tg mice initially showed a significant increase of LSGU at 12 W in GM of cervical and lumbar cords (Table 3; Figures 2Q–AB and Figures 3J–3R). However, LSGU now turned a progressive decrease from 16 to 19 W (Figures 3J–3R, black bars). The LSGU/SBF ratio showed a significant and continuous increase in GM of cervical, thoracic, and lumbar cords from 12 to 19 W of Tg mice (Figures 3S–AA).

Zhong *et al* (2008) showed a reduction of SBF in the cervical and lumbar cord as a whole in the same mice model of ours, but did not examine detailed regional differences and throughout the course before and after the disease onset. Decrease of cerebral blood flow was reported in ALS patients (Abe *et al*, 1997; Ishikawa *et al*, 2007; Waldemar *et al*, 1992), but that of SBF has not been reported in the ALS patients. Capillary diameter, density, and RBC velocity are important parameters of SBF. Our *in vivo* optical study strongly suggests that such an SBF reduction (Table 2; Figures 2E–2P) was closely related to the decrease of capillary diameter, density, and RBC velocity (Figure 1), and the early SBF reduction from the presymptomatic stage at 12 W might provide chronic and progressive ischemic stress to the affected spinal cord as implicated by early increase of Hif-1α and vascular endothelial growth factor (Murakami *et al*, 2003; Xu *et al*, 2011).

Several reports have shown weight loss, hypermetabolism, and hyperlipidemia in ALS patients and the animal model, suggesting a disturbance of energy metabolism (Dupuis *et al*, 2011; Guo *et al*, 2000; Hatazawa *et al*, 1988). Amyotrophic lateral sclerosis patients showed a reduced glucose metabolism in their cerebral cortex (Dalakas *et al*, 1987; Ludolph *et al*, 1992; Waldemar *et al*, 1992). Amyotrophic lateral sclerosis model mice showed a slight but nonsignificant increase of LSGU in the spinal cord at presymptomatic stage with a significant reduction at the end stage (Browne *et al*, 2006). Blood flow and glucose metabolism are well coupled under physiological conditions in both the brain and spinal cord FMC, where blood flow increases in response to an increased glucose metabolism (Krafft *et al*, 2000; Lenz *et al*, 1999; Leybaert, 2005; Leybaert *et al*, 2007; Sokoloff, 1977; Weir *et al*, 2002; Zivin *et al*, 1982).

In the present study, we found four important aspects of flow–metabolism uncoupling (FMU) in ALS spinal cord. (1) Spinal blood flow was progressively reduced beginning before the disease onset, and did not couple to the increasing LSGU at 12 W (Figures 2D,2E and Figures 3A–3I). (2) The initial LSGU increase at presymptomatic stage was followed by the LSGU reduction after the disease onset, when SBF reduction seemed to be partially coupled (Figures 2Q–2AB and Figure 3J–3R). (3) The LSGU/SBF ratio, a good indicator of FMC, showed that a high LSGU with uncoupled SBF continued from presymptomatic to the end stage of ALS (Figures 3S–AA). (4) Such an FMU was found only in Tg mice, preferentially in GM (AH > DH) and LF (Figures 2 and 3), where pathological changes are the most prominent in this ALS mice. The increase of LSGU at 12 W might be compensatory mechanism against early depletion of ATP (Browne *et al*, 2006) probably accompanied by mitochondrial deficit and hyperactivation of synaptic terminal, both of which were observed before apparent motor neuron degeneration (Gordon *et al*, 2010; Sasaki *et al*, 2004). The initial high LSGU with SBF reduction could cause not only an absolute ischemia (absolute SBF reduction) but also a relative hypoxia (regardless of LSGU increase or decrease) in the spinal motor neurons, resulting in a strong hypoxic/oxidative damage and reactive inflammatory responses. Such an initial presymptomatic event to spinal motor neurons and the surrounding inflammatory responses could bring secondary and continuous damage to motor neurons after the disease onset (Figure 3).

Recent reports have demonstrated a damage of blood spinal cord barrier components (Garbuzova-Davis *et al*, 2007; Henkel *et al*, 2009; Ishikawa *et al*, 2007) of both ALS patients and the model mice. Vascular endothelium, neurons, and glial cells form a functional unit together, called NVU (del Zoppo, 2010; Zlokovic, 2008), and blood flow is regulated by modulating blood vessel diameter to couple to the demand of glucose metabolism depending on local neuronal activity (Dirnagl, 1997; Harder *et al*, 1998; Kuschinsky, 1997). We have previously shown that a disruption of NVU enhanced an acute ischemic brain damage (Yamashita *et al*, 2009) and aggravated ALS pathology in the model mouse (Miyazaki *et al*, 2011). We found that significant changes of SBF and LSGU were largely restricted to GM, where damage of NVU was also prominent. The constant increase of LSGU/SBF ratio (Figures 3S–3AA) regardless of initial increase of LSGU and the later decrease (Figures 3J–3R) strongly suggests a larger decline of SBF than LSGU increase/decrease (Figures 3S–3AA). Such a large decline of SBF could be accounted for this NVU disruption (Miyazaki *et al*, 2011), as well as decreasing capillary diameter and density cooperatively affecting the neurodegenerative process of ALS. We have previously shown that motor function was decreased after 15 W using rotarod test in the same line of this model mouse (Ohta *et al*, in press). Thus, aberrant changes of SBF and LSGU persuaded the initiation of motor function reduction, and then progressively decreased with disease progression.

In the present study, we first showed a progressive impairment of FMU in the spinal cord of ALS mice, preceding the sequential changes of the disease, which strongly correlated with the affected regions of ALS, and is strongly related to decreasing capillary diameter and density and to NVU disruption. Although the reason why the presence of SOD1 caused initial SBF reduction and LSGU increase has to be dissolved by further analysis, we conclude that this early FMU could profoundly involve in the whole disease process as a vascular factor of ALS pathology, and could be a potential target for therapeutic intervention of ALS.

Disclosure/conflict of interest

The authors declare no conflict of interest.

References

Abe K, Fujimura H, Toyooka K, Sakoda S, Yorifuji S, Yanagihara T (1997) Cognitive function in amyotrophic lateral sclerosis. *J Neurol Sci* 148:95–100

Aoki M, Ogasawara M, Matsubara Y, Narisawa K, Nakamura S, Itoyama Y, Abe K (1993) Mild ALS in Japan associated with novel SOD mutation. *Nat Genet* 5:323–4

Autio J, Kawaguchi H, Saito S, Aoki I, Obata T, Masamoto K, Kanno I (2011) Spatial frequency-based analysis of mean red blood cell speed in single microvessels: investigation of microvascular perfusion in rat cerebral cortex. *PLoS One* 6:e24056

Boillee S, Yamanaka K, Lobsiger CS, Copeland NG, Jenkins NA, Kassiotis G, Kollias G, Cleveland DW (2006) Onset and progression in inherited ALS determined by motor neurons and microglia. *Science* 312:1389–92

Browne SE, Yang L, DiMauro JP, Fuller SW, Licata SC, Beal MF (2006) Bioenergetic abnormalities in discrete cerebral motor pathways presage spinal cord pathology in the G93A SOD1 mouse model of ALS. *Neurobiol Dis* 22:599–610

Clement AM, Nguyen MD, Roberts EA, Garcia ML, Boillee S, Rule M, McMahon AP, Doucette W, Siwek D, Ferrante RJ, Brown Jr RH, Julien JP, Goldstein LS, Cleveland DW (2003) Wild-type nonneuronal cells extend survival of SOD1 mutant motor neurons in ALS mice. *Science* 302:113–7

Dalakas MC, Hatazawa J, Brooks RA, Di Chiro G (1987) Lowered cerebral glucose utilization in amyotrophic lateral sclerosis. *Ann Neurol* 22:580–6

Davalos D, Lee JK, Smith WB, Brinkman B, Ellisman MH, Zheng B, Akassoglou K (2008) Stable *in vivo* imaging of densely populated glia, axons and blood vessels in the mouse spinal cord using two-photon microscopy. *J Neurosci Methods* 169:1–7

del Zoppo GJ (2010) The neurovascular unit, matrix proteases, and innate inflammation. *Ann NY Acad Sci* 1207:46–9

Dirnagl U (1997) Metabolic aspects of neurovascular coupling. *Adv Exp Med Biol* 413:155–9

Dupuis L, Pradat PF, Ludolph AC, Loeffler JP (2011) Energy metabolism in amyotrophic lateral sclerosis. *Lancet Neurol* 10:75–82

Garbuzova-Davis S, Saporta S, Haller E, Kolomey I, Bennett SP, Potter H, Sanberg PR (2007) Evidence of compromised blood-spinal cord barrier in early and late symptomatic SOD1 mice modeling ALS. *PLoS One* 2:e1205

Gordon T, Tyreman N, Li S, Putman CT, Hegedus J (2010) Functional over-load saves motor units in the SOD1-G93A transgenic mouse model of amyotrophic lateral sclerosis. *Neurobiol Dis* 37:412–22

Guo Z, Kindy MS, Kruman I, Mattson MP (2000) ALS-linked Cu/Zn-SOD mutation impairs cerebral synaptic glucose and glutamate transport and exacerbates ischemic brain injury. *J Cereb Blood Flow Metab* 20:463–8

Gurney ME, Pu H, Chiu AY, Dal Canto MC, Polchow CY, Alexander DD, Caliendo J, Hentati A, Kwon YW, Deng HX, Chen W, Zhai P, Sufit RL, Siddique T (1994) Motor neuron degeneration in mice that express a human Cu,Zn superoxide dismutase mutation. *Science* 264:1772–5

Harder DR, Alkayed NJ, Lange AR, Gebremedhin D, Roman RJ (1998) Functional hyperemia in the brain: hypothesis for astrocyte-derived vasodilator metabolites. *Stroke* 29:229–34

Hatazawa J, Brooks RA, Dalakas MC, Mansi L, Di Chiro G (1988) Cortical motor-sensory hypometabolism in amyotrophic lateral sclerosis: a PET study. *J Comput Assist Tomogr* 12:630–6

Henkel JS, Beers DR, Wen S, Bowser R, Appel SH (2009) Decreased mRNA expression of tight junction proteins in lumbar spinal cords of patients with ALS. *Neurology* 72:1614–6

Ishikawa T, Morita M, Nakano I (2007) Constant blood flow reduction in premotor frontal lobe regions in ALS with dementia - a SPECT study with 3D-SSP. *Acta Neurol Scand* 116:340–4

Jay TM, Lucignani G, Crane AM, Jehle J, Sokoloff L (1988) Measurement of local cerebral blood flow with [14C]iodoantipyrine in the mouse. *J Cereb Blood Flow Metab* 8:121–9

Krafft P, Frietsch T, Lenz C, Piepgras A, Kuschinsky W, Waschke KF (2000) Mild and moderate hypothermia (alpha-stat) do not impair the coupling between local cerebral blood flow and metabolism in rats. *Stroke* 31:1393–400; discussion 401

Kuschinsky W (1997) Neuronal-vascular coupling. A unifying hypothesis. *Adv Exp Med Biol* 413:167–76

Lenz C, Frietsch T, Futterer C, Rebel A, van Ackern K, Kuschinsky W, Waschke KF (1999) Local coupling of cerebral blood flow to cerebral glucose metabolism during inhalational anesthesia in rats: desflurane versus isoflurane. *Anesthesiology* 91:1720–3

Leybaert L (2005) Neurobarrier coupling in the brain: a partner of neurovascular and neurometabolic coupling? *J Cereb Blood Flow Metab* 25:2–16

Leybaert L, De Bock M, Van Moorhem M, Decrock E, De Vuyst E (2007) Neurobarrier coupling in the brain: adjusting glucose entry with demand. *J Neurosci Res* 85:3213–20

Llinas RR, Sugimori M, Moran KA, Moreira JE, Fukuda M (2004) Vesicular reuptake inhibition by a synaptotagmin I C2B domain antibody at the squid giant synapse. *Proc Natl Acad Sci USA* 101:17855–60

Lo EH, Rosenberg GA (2009) The neurovascular unit in health and disease: introduction. *Stroke* 40:S2–3

Ludolph AC, Langen KJ, Regard M, Herzog H, Kemper B, Kuwert T, Bottger IG, Feinendegen L (1992) Frontal lobe function in amyotrophic lateral sclerosis: a neuropsychologic and positron emission tomography study. *Acta Neurol Scand* 85:81–9

Miyazaki K, Ohta Y, Nagai M, Morimoto N, Kurata T, Takehisa Y, Ikeda Y, Matsuura T, Abe K (2011) Disruption of neurovascular unit prior to motor neuron degeneration in amyotrophic lateral sclerosis. *J Neurosci Res* 89:718–28

Murakami T, Ilieva H, Shiote M, Nagata T, Nagano I, Shoji M, Abe K (2003) Hypoxic induction of vascular endothelial growth factor is selectively impaired in mice carrying the mutant SOD1 gene. *Brain Res* 989:231–7

Murakami T, Nagai M, Miyazaki K, Morimoto N, Ohta Y, Kurata T, Takehisa Y, Kamiya T, Abe K (2007) Early decrease of mitochondrial DNA repair enzymes in spinal motor neurons of presymptomatic transgenic mice carrying a mutant SOD1 gene. *Brain Res* 1150: 182–9

Nagai M, Re DB, Nagata T, Chalazonitis A, Jessell TM, Wichterle H, Przedborski S (2007) Astrocytes expressing ALS-linked mutated SOD1 release factors selectively toxic to motor neurons. *Nat Neurosci* 10:615–22

Ohta Y, Nagai M, Miyazaki K, Tanaka T, Kawai H, Morimoto N, Kurata T, Ikeda Y, Matsuura T, Abe K. Neuroprotective and angiogenic effects of bone marrow transplantation combined with granulocyte colony-stimulating factor in a mouse model of amyotrophic lateral sclerosis. *Cell Transplantation* (in press)

Pramatarova A, Laganiere J, Roussel J, Brisebois K, Rouleau GA (2001) Neuron-specific expression of mutant superoxide dismutase 1 in transgenic mice does not lead to motor impairment. *J Neurosci* 21:3369–74

Rosen DR, Siddique T, Patterson D, Figlewicz DA, Sapp P, Hentati A, Donaldson D, Goto J, O'Regan JP, Deng HX, Rahmani Z, Krizus A, McKenna-Yasek D, Cayabyab A, Gaston SM, Berger R, Tanzi RE, Halperin JJ, Herzfeldt B, Van den Bergh R, Hung WY, Bird T, Deng G, Mulder DW, Smyth C, Laing NG, Soriano E, Pericak-Vance MA, Haines J, Rouleau GA, Gusella JS, Horvitz HR, Brown RH (1993) Mutations in Cu/Zn superoxide dismutase gene are associated with familial amyotrophic lateral sclerosis. *Nature* 362:59–62

Sakurada O, Kennedy C, Jehle J, Brown JD, Carbin GL, Sokoloff L (1978) Measurement of local cerebral blood flow with iodo [14C] antipyrine. *Am J Physiol* 234:H59–66

Sasaki S, Warita H, Murakami T, Abe K, Iwata M (2004) Ultrastructural study of mitochondria in the spinal cord of transgenic mice with a G93A mutant SOD1 gene. *Acta Neuropathol* 107:461–74

Sokoloff L (1977) Relation between physiological function and energy metabolism in the central nervous system. *J Neurochem* 29:13–26

Waldemar G, Vorstrup S, Jensen TS, Johnsen A, Boysen G (1992) Focal reductions of cerebral blood flow in amyotrophic lateral sclerosis: a [99mTc]-d,l-HMPAO SPECT study. *J Neurol Sci* 107:19–28

Wang J, Xu G, Slunt HH, Gonzales V, Coonfield M, Fromholt D, Copeland NG, Jenkins NA, Borchelt DR (2005) Coincident thresholds of mutant protein for paralytic disease and protein aggregation caused by restrictively expressed superoxide dismutase cDNA. *Neurobiol Dis* 20:943–52

Weir CJ, Zivin JA, Lyden PD (2002) Inter-relationships between spinal cord blood flow, neuronal death and neurological function in rabbit spinal cord ischemia. *Brain Res* 946:43–51

Xu R, Wu C, Zhang X, Zhang Q, Yang Y, Yi J, Yang R, Tao Y (2011) Linking hypoxic and oxidative insults to cell death mechanisms in models of ALS. *Brain Res* 1372:133–44

Yamashita T, Kamiya T, Deguchi K, Inaba T, Zhang H, Shang J, Miyazaki K, Ohtsuka A, Katayama Y, Abe K (2009) Dissociation and protection of the neurovascular unit after thrombolysis and reperfusion in ischemic rat brain. *J Cereb Blood Flow Metab* 29:715–25

Zhong Z, Deane R, Ali Z, Parisi M, Shapovalov Y, O'Banion MK, Stojanovic K, Sagare A, Boillee S, Cleveland DW, Zlokovic BV (2008) ALS-causing SOD1 mutants generate vascular changes prior to motor neuron degeneration. *Nat Neurosci* 11:420–2

Zivin JA, DeGirolami U, Hurwitz EL (1982) Spectrum of neurological deficits in experimental CNS ischemia. A quantitative study. *Arch Neurol* 39:408–12

Zlokovic BV (2008) The blood-brain barrier in health and chronic neurodegenerative disorders. *Neuron* 57: 178–201

Experimental Pig Model of Old Myocardial Infarction with Long Survival Leading to Chronic Left Ventricular Dysfunction and Remodeling as Evaluated by PET

Noboru Teramoto[1], Kazuhiro Koshino[1], Ikuo Yokoyama[2,3], Shigeru Miyagawa[4], Tsutomu Zeniya[1], Yoshiyuki Hirano[1], Hajime Fukuda[1], Junichiro Enmi[1], Yoshiki Sawa[4], Juhani Knuuti[5], and Hidehiro Iida[1]

[1]Department of Investigative Radiology, National Cerebral and Cardiovascular Center Research Institute, Osaka, Japan; [2]School of Medicine and Faculty of Medicine, University of Tokyo, Tokyo, Japan; [3]Department of Cardiovascular Medicine, Sanno Hospital, International University of Health and Welfare, Tokyo, Japan; [4]Department of Cardiac Surgery, Osaka University, School of Medicine, Osaka, Japan; and [5]Turku PET Centre, University of Turku, Turku, Finland

A pig model of reduced left ventricular (LV) function and remodeling or chronic heart failure with long survival after myocardial infarction (MI) has not been established. The aim of this study was to evaluate the pathophysiologic status of a pig model of old MI using a series of PET studies. **Methods:** Twenty-seven male farm pigs were divided into 2 groups: 7 animals in the control group and 20 animals that underwent a proximal coronary artery (CA) occlusion using an ameroid constrictor after distal CA ligation. A series of PET examinations was performed to assess LV volumes, LV functions, myocardial perfusion response to adenosine, and viability as water-perfusable tissue index. **Results:** The distal CA ligation inhibited arrhythmia during and after the operation, and a transmural anteroseptal MI, with an infarction area of 27% ± 5% of the whole left ventricle, was generated with a survival rate of 75% at 4 mo. Wall motion evaluated by ^{18}F-FDG PET was diffusely reduced, including the noninfarcted wall. Global LV ejection fraction as assessed by gated C^{15}O PET was reduced (39% ± 16%) in the group undergoing occlusion, compared with the control group (66% ± 16%, $P < 0.05$). LV end-systolic (31.4 ± 9.2 cm^3) and end-diastolic (52.7 ± 10.2 cm^3) volumes were increased, compared with controls (15.2 ± 9.4 cm^3, $P < 0.01$, and 41.7 ± 11.5 cm^3, $P < 0.05$, respectively). Histology showed hypertrophy and development of microscopic fibrosis in noninfarcted myocardium. PET demonstrated the reduced myocardial perfusion response to adenosine and also reduced water-perfusable tissue index in remote segments. **Conclusion:** The pig model of old MI generated by the chronic proximal CA obstruction after distal ligation was characterized by LV dysfunction and remodeling, with a high survival rate.

Key Words: experimental model; PET; myocardial flow reserve; remodeling; regeneration therapy

J Nucl Med 2011; 52:761–768
DOI: 10.2967/jnumed.110.084848

Received Oct. 30, 2010; revision accepted Dec. 9, 2010.
For correspondence or reprints contact: Hidehiro Iida, Department of Investigative Radiology, National Cardiovascular Center Research Institute, 5-7-1 Fujishiro-dai, Suita City, Osaka, Japan 565-8565.
E-mail: iida@ri.ncvc.go.jp

Chronic heart failure (CHF) is an increasing health concern (*1*). Myocardial infarction (MI) is the cause of CHF in two thirds of the patients, and the morbidity and mortality remain high (*2,3*). The potential therapies, such as new class of pharmacologic agents and cell therapy (*4*), need to be tested in proper animal models to demonstrate the effects and outcome before initiating clinical trials. Dogs have been extensively used in heart research. Because the coronary arterial systems in dogs can develop collaterals quickly when myocardial ischemia occurs, it has been difficult to produce a large MI that typically introduces CHF with general characteristics of left ventricular (LV) remodeling (*5*).

Pigs have been considered better suited than dogs for pathophysiologic research of ischemic heart diseases, because the coronary system of pigs is more similar to that of humans (*6*). Tolerance of ischemia and denervation after ischemia in pigs is also similar to that in humans (*6*). Because of the delayed development of collaterals after occlusion, ligation of a peripheral part of the coronary arterial system generates a small MI (*7*). However, an experimental model of large MI introducing global LV dysfunction is difficult to develop, because sudden cardiac death (SCD) due to fatal arrhythmias and an intolerance of ischemia frequently occurs in pigs (*8*). The models of small MI made by the ligation of a peripheral part of the coronary arterial system demonstrate reasonably good survival rates but only for a small infarction. The model of small MI using a coronary ameroid constrictor (model MRI-2.50-TI; Research Instruments SW) has also demonstrated moderate SCD rates (*6,8–13–15*), but the animals develop primarily chronic ischemia or hibernating myocardium, without a significant amount of scar tissue. Thus, the limitations of current models are that the infarcted region is small and that the hearts are not developing a clinical picture of CHF with global LV dysfunction, LV dilatation, and remodeling.

On the other hand, Shen et al. (*16*) developed an experimental pig model of MI and heart failure. Sequential

ligation of distal and proximal coronary arteries was used to establish MI with a reasonable survival rate, and pacing tachycardia was used to achieve heart failure. However, this pig model was studied over only a short term (21 d) and required pacing tachycardia to cause CHF. There has been little evaluation of pathophysiology and no evidence of the presence of cardiac remodeling.

This aim of this study was to characterize the pig model of old MI. We first reinvestigated the technique of generating a pig model of relatively large MI causing global LV dysfunction and LV remodeling in segments remote from the infarcted region, by means of the sequential ligation of distal and proximal coronary arteries without the pacing procedures. We then evaluated the pathophysiologic characteristics of this animal model by comprehensively analyzing histology, LV volumes and LV function, myocardial perfusion response to adenosine, and perfusable tissue fractions (PTF) in the remote segment, using an advanced PET technique.

MATERIALS AND METHODS

Subjects

Male farm pigs, 3 mo old at the start of the study (weight range, 18–23 kg; mean weight ± SD, 20 ± 1.2 kg), were used. The animals were divided into 2 groups. Group A consisted of 7 pigs without any operation and was designated as the control group (average body weight, 26 ± 2.4 kg). Group B consisted of 20 pigs that underwent occlusion using an ameroid constrictor (*7*); ligation of the distal left anterior descending coronary artery (LAD) was performed before the ameroid constrictor was used. Of the 16 pigs that survived for 4 mo after the operation, 7 underwent PET studies. The other 9 were assigned to tissue-regenerative projects. The average body weight of this group of 7 pigs was 42 ± 8.2 kg at the time of the PET scan.

Animals were maintained and handled in accordance with guidelines for animal research (*17*). The study protocol was approved by the local Committee for Laboratory Animal Welfare, National Cardiovascular Center, Osaka, Japan.

Permanent Occlusion Procedures

In group B, permanent occlusion was made at the proximal LAD using an ameroid constrictor (*18*) (Fig. 1) as follows. Pigs were preanesthetized by an intramuscular injection of ketamine hydrochloride (20 mg/kg; Ketaral [Diichi-Sankyo]) and xylazine hydrochloride (2 mg/kg; Celactal [Bayer HealthCare]). The animals were positioned supine, and a 22-gauge indwelling needle (Surflo F&F; Terumo) was inserted in the central vein of the auricle. A 3-way cock (Terufusion TS-TR2K; Terumo) was attached to the external cylinder of the indwelling needle and connected for continuous anesthetic injection. The animals were intubated with an endotracheal cannula (6 French; Sheridan) and then connected to an artificial respirator (Single Animal Volume Controlled Ventilators model 613 [Harvard Apparatus]) with a stroke volume of 200–300 cm^3/stroke and frequency of 20/min. Propofol (6 mg/kg/h; Diprivan [Astra-Zeneca]) and vecuronium bromide (0.05 mg/kg/h; Musculux [Sankyo Yell Yakuhin Co., Ltd.]) were continuously infused using a syringe pump (Terufusion TE-3310N; Terumo). Then, the animals were fixed in a recumbent position so that the left thorax was exposed, and the outer layer of skin and muscles between the third and fourth ribs was dissected. The distance between the third and fourth ribs was widened with a rib spreader to allow a direct view of the left auricle and LAD. The pericardium was dissected along the LAD, from the upper part of the left auricle (~6 cm), to expose the myocardium around the LAD. The LAD on the proximal side, below the left auricle from the myocardium, was exfoliated for approximately 1 cm. A lidocaine hydrochloride jelly (Xylocaine jelly; Astra-Zeneca) was applied to anesthetize the area.

A complete ligation was first made on the distal LAD (no. 9), immediately after the second diagonal branch, using a suture (2-0; Nescosuture) approximately 20 min before the ameroid constrictor was fastened. An ameroid constrictor (COR-2.50-SS; Research Instruments) was then fastened using sutures as displayed in Figure 1. To enhance the effect of the ameroid constrictor, 2 additional suture strings were loosely rounded at the site of the ameroid so that these strings were located between (below) the ameroid constrictor and arterial wall.

PET Procedures

After fasting overnight, the pigs were sedated with ketamine hydrochloride (20 mg/kg) and xylazine hydrochloride (2 mg/kg) by intramuscular injection. Anesthesia was induced and maintained with intravenous propofol (6 mg/kg/h) and vecuronium bromide (0.05 mg/kg/h). The animals were intubated and mechanically ventilated with a mixture of 25% oxygen and 75% nitrogen at 10 mL/kg plus 50 mL/stroke at 20 strokes/min. Catheters were placed in the femoral artery to monitor the arterial blood pressure and in the femoral vein to infuse $H_2{}^{15}O$ or ^{18}F-labeled FDG. Systolic and diastolic blood pressure, heart rate, and arterial blood gases were monitored.

A series of PET scans was obtained using an ECAT-HR tomograph (CTI Inc.). The blood-pool images were obtained after the animals inhaled 2.7 GBq of $C^{15}O$ gas (*19*). Arterial blood samples were taken every minute during the $C^{15}O$ scan, and their radioactivity concentration in the whole blood was measured. Additional electrocardiogram-gated $C^{15}O$ images were obtained (16 gates). After 12–15 min of ^{15}O radioactivity decay, 7 dynamic $H_2{}^{15}O$ PET scans were acquired at intervals of 12–15 min. The first and the last scans were obtained without pharmacologic stress, and the second through sixth scans were obtained during intravenous infusion of adenosine (100, 200, 400, 600, and 800

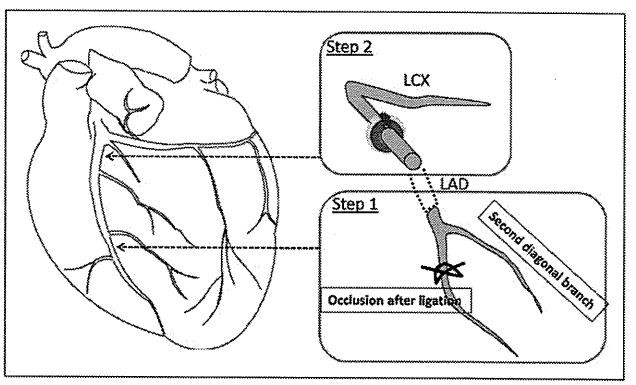

FIGURE 1. Ligation of LV LAD. Distal LAD after second diagonal branch was ligated, and 30 min later ameroid constrictor was placed at proximal LAD. Two suture strings were inserted between ameroid constrictor and arterial wall to make occlusion complete. LCX = left circumflex artery.

[only for group A] μg/kg/min). The 6-min dynamic scan of 26 frames (12 × 5, 8 × 15, and 6 × 30 s) was started when radioactivity appeared in the right ventricle. Furthermore, another PET scan using ^{18}F-FDG was acquired using a euglycemic hyperinsulinemic clamp (*20,21*). For this study, insulin (4 mIU/kg/h) and glucose (5–8 mg/kg/min) were continuously infused over 2 h, and then approximately 111 MBq of ^{18}F-FDG was intravenously injected. The blood glucose was 109 ± 10.6, 105 ± 3.8, and 107 ± 10.0 mg/dL at the time of ^{18}F-FDG injection. PET images were acquired dynamically for 60 min, and the images acquired during the last 30 min were used for further analysis. An additional electrocardiogram-gated scan was obtained for 30 min to estimate myocardial wall motion and wall thickening.

After the PET scans, coronary angiography was undertaken to confirm the occlusion of LAD. A portable angiographic camera (Digital Mobile Imaging System OEC Series 9800; GE Healthcare U.K. Ltd.) was used with the contrast medium (Omnipaque 300; Daiichi-Sankyo).

Histologic Analysis

At the end of the study, pentobarbital sodium was administered, and animals were euthanized. The animals' hearts were then excised and sliced at a thickness of 10 mm to correspond to PET images (*22*). The slices were stained with Masson trichrome and hematoxylin and eosin. The surface area of the infarcted LV wall on the stained slices was calculated according to a previously describe procedure (*22*). The length of the infarcted zone, including both transmural and nontransmural infarction, was measured on each of the stained slices along the LV wall. The defect surface area was then calculated as a summation of the defect length multiplied by the slice interval. The cell and microvascular structures were also analyzed. In particular, development of fibrosis, cell enlargement, and degeneration of the vascular network were visually estimated. The analysis was masked from the other analyses.

Data Analysis

The extravascular tissue density images (g/mL) were calculated by subtracting the $C^{15}O$ blood volume from the transmission images (*23*). The relative images of myocardial blood flow (MBF) and water-PTF (g/mL) were also generated from the dynamic $H_2{}^{15}O$ images (*22,23*). The relative accumulation of ^{18}F-FDG was calculated using validated techniques (*24*). The regions of interest were placed in the anterior wall and lateral–anterior wall, which corresponded to the MI and normal-tissue regions, respectively. The regions of interest were then copied to other images, and the quantitative parameters of regional MBF (mL/min/g), PTF (g/mL), and arterial blood volume V_a (mL/mL) were calculated using nonlinear least-squares fitting as described previously (*22,23*). These calculations were done for all $H_2{}^{15}O$ PET studies to estimate baseline MBF and the adenosine-based responses both in MI and in non-MI regions.

The water-perfusable tissue index (PTI) (*23,25,26*), which was defined as the fraction of water-perfusable tissue over total tissue, was calculated by dividing PTF by the extravascular tissue density images. This calculation was done for each myocardial region and compared between the infarcted anterior wall and normal posterior–lateral wall regions. The obtained values were also compared with control subjects.

The LV ejection fraction and cardiac output were evaluated by counting the total counts within the LV area from the typical electrocardiogram-gated $C^{15}O$ images shown in Figure 2. The wall motion was analyzed using electrocardiogram-gated ^{18}F-FDG images. The wall motion score was divided into 4 levels (normal, 0; hypokinetic, 1; akinetic, 2; and dyskinetic, 3) and defined for the anterior wall and contralateral (lateral–posterior) wall regions.

The surface area of the infarcted LV wall on the ^{18}F-FDG and PTF images was calculated as described previously (*22*). A significant defect was defined as a value less than 50% of that in the control region, which was defined in the contralateral region, indicating preserved ^{18}F-FDG, preserved PTF, and elevated MBF during adenosine. The myocardial midlines were then traced along the 50% of peak count boundary of the $C^{15}O$ blood volume images at each slice (*22*). The surface area of the defect was calculated as a summation of the defect length multiplied by the slice interval. These defect surface areas were compared with those obtained from the stained slices.

All data were presented as mean ± SD. Pearson correlation and linear regression analyses were used to evaluate relationships between the 2 values. A P value of less than 0.05 was considered statistically significant.

RESULTS

Survival Rates of Animal Groups

No adverse events were detected in group A; in group B, 4 pigs (20%) died within a month and an additional pig 1 mo after that. Thus, the total survival rate at 4 mo was 75% in group B. Severe arrhythmia occurred in all animals in group B during the operation. The arrhythmia and fibrillation, introducing the sudden cardiac death, were significantly suppressed at approximately 20 min after ligation of the distal LAD. Figure 3 displays the survival rates of the pigs that underwent the operation.

Of the pigs in group B that survived for 4 mo, 7 were selected for further characterization and imaging studies. These 7 animals were compared against the animals in group A, on which no operation was performed. The characteristics of the 2 groups at the time of the imaging

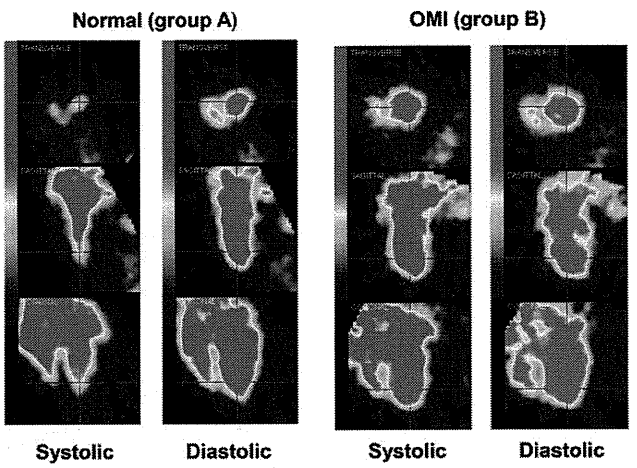

FIGURE 2. Typical images obtained from electrocardiogram-gated PET scans with $C^{15}O$ inhalation at end-systolic and end-diastolic phases. OMI = old MI.

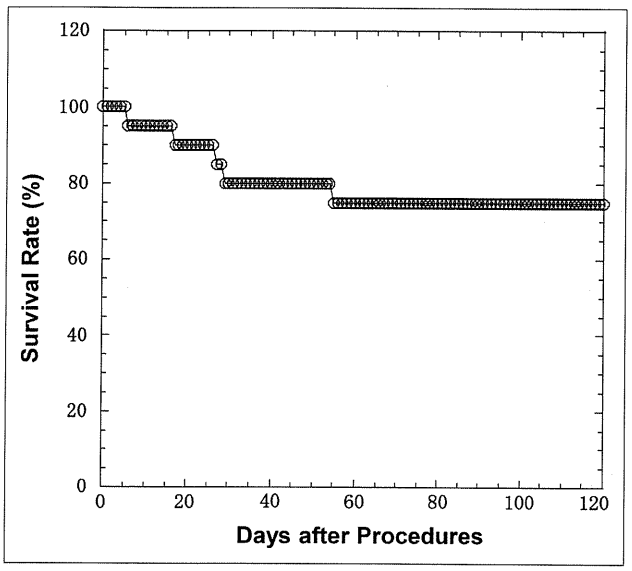

FIGURE 3. Survival rates for group B after ameroid constrictor was placed.

studies are displayed in Table 1. Because the animals in group B were allowed to grow after operation, they were larger at the time of the imaging studies.

Characteristics of Groups

Table 1 shows the hemodynamic data for the animals in groups A and B. Compared with group A, group B showed a significantly reduced heart rate and diastolic blood pressure and, thus, rate–pressure product. In addition, the global LV ejection fraction measured with gated $C^{15}O$ PET in group B was significantly reduced (39% ± 16% [24%–59%] in group B vs. 66% ± 16% [46%–91%] in group A, $P < 0.01$). LV end-systolic volume in group B was significantly increased (31.4 ± 9.2 cm^3 in group B vs. 15.2 ± 9.4 cm^3 in group A, $P < 0.01$), and LV end-diastolic volume was also significantly increased (52.7 ± 10.2 cm^3 in group B vs. 41.7 ± 11.5 cm^3 in group A, $P < 0.05$). Increased end-systolic and end-diastolic volumes are also clearly visible in Figure 2. Systolic blood pressure and diastolic blood pressure, as well as rate–pressure product, were reduced during adenosine study in both groups. Heart rate was increased in group A but not in group B. Other parameters such as hemoglobin concentration (g/dL), percentage saturation of arterial O_2, $PaCO_2$ (mm Hg), and PO_2 (mm Hg) were not significantly different between the 2 groups. Table 2 shows detailed hemodynamic parameters and the results from the histologic analysis for each individual animal in group B. Wall motion score was reduced (akinesis–dyskinesis or 2–3) in the anterior wall, which includes the area of MI. The wall motion score was also reduced diffusely in all animals and indicated hypokinesis (grade 1) in the infarct-remote posterolateral wall. The coronary angiography demonstrated complete occlusion of the LAD in all animals in group B. As shown in Figure 4, no clear collateral circulation existed.

Imaging Results

The myocardial perfusion ($H_2{}^{15}O$) and metabolism (^{18}F-FDG) images at the mid ventricular plane and their corresponding slices after histochemical staining for the animals in group B are displayed in Figure 5. In all animals, clear signs of MI were detected in the anterior wall. The surface area of the MI was 13.7 ± 4.3 cm^2, which corresponded to 27% ± 9% of the whole left ventricle. Both PTF and ^{18}F-FDG images visually agreed well with the stained slices. Moreover, the ^{18}F-FDG images agreed well with the qualitative PTF images in all animals. The spatial distribution and size of the developed MI are visually reproducible

TABLE 1
Physiologic Parameters of Pigs at Time of PET

Parameter	Group A (control, n = 7)	Group B (old MI, n = 7)
Body weight (kg)	26 ± 2.4	41 ± 8.2
Heart rate (beats·min^{-1})	72 ± 22.4 (82 ± 21.4*)	52 ± 6.3† (53 ± 9.2)
Systolic blood pressure (mm Hg)	131 ± 22.1 (95 ± 22.4‡)	111 ± 18.3† (97 ± 15.0*)
Diastolic blood pressure (mm Hg)	92 ± 19.3 (49 ± 16.7‡)	74 ± 13.6† (57 ± 11.9‡)
Rate pressure product (mm Hg·min^{-1})	9,567 ± 3,616 (5,657 ± 3201‡)	5,732 ± 1,151† (4,445 ± 948*)
Wall thickness (posterior–lateral wall) (cm)	1.2 ± 0.1	1.6 ± 0.1‡
End-diastolic LV volume (mL)	41.7 ± 11.5	52.73 ± 10.2†
End-systolic LV volume (mL)	15.2 ± 9.4	31.4 ± 9.2*
LV ejection fraction (%)	66.0 ± 16.2	39.7 ± 16.9*
Hemoglobin concentration (g/dL)	13 ± 1.5	12 ± 0.9
Saturation of arterial O_2 (%)	99 ± 1.0	99 ± 0.6
pCO_2 (mm Hg)	39 ± 2.7	41 ± 2.8
pO_2 (mm Hg)	125 ± 20.1	141 ± 11.4

*$P < 0.01$.
†$P < 0.05$.
‡$P < 0.001$.
Data are mean ± SD. Values in parentheses are from administration of maximum dose of adenosine.

TABLE 2
Hemodynamic Parameters of Pigs with Old MI (Group B)

Subject no.	BW (kg)	HR (beats·min^{-1})	SBP (mm Hg)	DBP (mm Hg)	RPP (mm Hg·min^{-1})	tHb (g/dL)	SAT (%)	pCO_2 (mm Hg)	pO_2 (mm Hg)	WM							
										Anterior wall	Posterior–lateral wall	WT (posterior–lateral wall)	EDV (mL)	ESV (mL)	EF (%)	LV surface area (cm^2)	MI surface area (cm^2)	DAF (%)
1	37	53	117	72	6,201	10.8	98.7	37.8	132	3	1	1.6	39.5	29.9	24.3	53.7	10.9	20.3
2	39	38	110	70	4,180	11.5	98.9	37	154.5	2	1	1.6	58.2	42.4	27.1	57	16.2	28.4
3	33	53	85	60	4,505	11.5	99.3	39.3	137.7	3	1	1.6	55.4	42.3	23.6	50	16	31.9
4	32	55	91	58	5,005	11.3	99.6	40.7	135.5	–	–	1.8	0	0	0	53.9	9.2	17.1
5	45	52	137	93	7,124	10.3	98.1	43.6	124.1	3	1	1.8	68.4	27.6	59.7	50	19.9	39.7
6	50	52	126	90	6,552	11.8	99.7	42.8	148.4	3	1	1.5	49.3	27.1	45	48.6	15.5	31.8
7	53	58	113	78	6,554	13.3	99	43.7	152.8	2	1	1.5	45.7	19.1	58.2	49.8	8.4	16.9
Mean	41	52	111	74	5,732	12	99	41	141	2.7	1	1.6	52.7	31.4	39.7	51.9	13.7	26.6
SD	8.2	6.3	18.3	13.6	1,151	0.9	0.6	2.8	11.4	0.5	0	0.1	10.2	9.2	16.9	3.05	4.3	8.7

BW = body weight; HR = heart rate; SBP = systolic blood pressure; DBP = diastolic blood pressure; RPP = rate–pressure product; tHB = hemoglobin concentration; SAT = saturation of arterial O_2; WM = wall motion; WT = wall thickness; EDV = end-diastolic LV volume; ESV = end-systolic LV volume; EF = ejection fraction; DAF = defect area fraction.

FIGURE 4. Example of coronary angiogram in animal with ameroid constrictor (arrow) (group B).

among the animals. Myocardial hypertrophy was visible in the wall regions remote from the infarcted area. In group B, the posterior–lateral wall thickness estimated from histochemical staining was 16 ± 1 mm (Table 2), which was significantly greater than that of group A (12 ± 1 mm; Table 1) ($P < 0.001$).

Further analysis of the size of the infarcted region is displayed in Figure 5B. We excluded 1 animal whose ^{18}F-FDG PET images demonstrated high accumulation at the anterior LV area (and therefore a smaller value in the defect surface area), which was attributed to the adhesion or inflammation between the myocardial and chest walls. Thus, the defect area on histology showed intersubject variation of approximately 20%. The results of both ^{18}F-FDG and PTF image analysis and histochemical analysis agreed well (Fig. 5B). Baseline and adenosine-stimulated MBF were also clearly blunted in the anterior wall in the animals in group B (Fig. 6A). Interestingly, abnormally reduced adenosine flow response also was detected in the myocardial regions remote from the MI in group B, whereas the baseline flow values were normal.

Further analysis of myocardial PTF and PTI values—indices of PTF—revealed that these values were significantly reduced in the infarcted anterior wall in group B (Fig. 6B). PTI was also moderately but significantly (~10%) reduced in the remote myocardial wall in group B.

Histologic Analysis

Histologic analysis did not show any signs of MI in group A, but transmural anterior wall MI was apparent in all animals in group B. Hypertrophy was detected in the posterior wall of group B in all animals. Multinuclear muscle cell breeding (Fig. 7A) and hyperplasia of blood vessels (Fig. 7B) were also visible in all animals in group B, mostly in the subendocardial regions. Denaturation necrosis with epicardial fibrous change and hypertrophy has also been seen in the lateral–posterior wall regions of group B (Fig. 7C).

DISCUSSION

This study demonstrated that 75% of pigs with old MI generated by the 2 steps of LAD ligation survived more than 4 mo. Such a long survival has never, to our

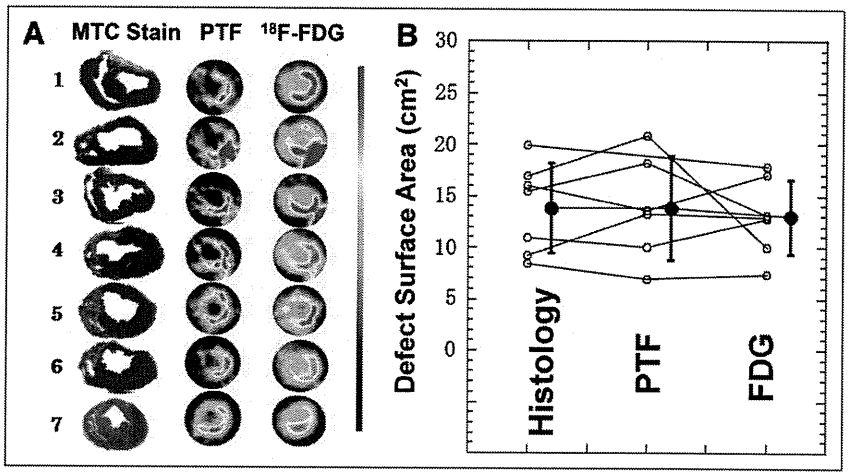

FIGURE 5. (A) Histologic, PTF, and ^{18}F-FDG slices at middle level of left ventricle in 7 animals of group B. Spatial distribution and size of MI are visually reproducible among animals. Myocardial hypertrophy was visible in remote myocardial wall regions. (B) Comparison of defect surface areas obtained from histologic stained slices with PET images using ^{18}F-FDG and PTF. MTC = Masson trichrome.

knowledge, been accomplished in any studies of pig heart disease. The size of MI reached approximately 27% of the whole left ventricle, causing the remodeling and global LV dilatation (significantly increased LV end-systolic and end-diastolic volumes) to be associated with reduced global LV function. PET with $C^{15}O$ and ^{18}F-FDG showed that regional LV wall motion was impaired not only in the infarcted region but also in the myocardial areas remote from the MI. PET also demonstrated reduced MBF reactivity in remote regions in addition to the infarct area. PTI was also reduced in the remote region, suggesting development of microscopic fibrosis. Moreover, other findings from histology indicated the existence of abnormalities in the noninfarcted area remote from the MI. These results indicate that this animal model may be close to human CHF after MI.

Shen et al. (*16*) adopted additional pacing tachycardia in pigs after sequential coronary artery ligations and observed global LV dysfunction, claiming that CHF was introduced. The present study is similar to the study by Shen et al. (*16*) but is based on only sequential coronary artery obstructions accomplished with acute distal coronary artery occlusion followed by a chronic proximal coronary occlusion with an ameroid constrictor, causing similar LV dysfunction. Of note was the better survival rate (80% at 1 mo, 75% at 4 mo) demonstrated in the current report than in any previous report (*6,8–12,14,16*), including Shen et al. (73.3% at 21 d). In addition, it has not been confirmed whether such a good survival rate at 21 d could last more than 4 mo after producing global LV dysfunction with MI. Our preliminary experiment, independently performed on 69 farm pigs, demonstrated that when the proximal LAD was occluded by the ameroid constrictor alone, 45 pigs (65%) died within a month, and the total survival rate was 30% at 4 mo. This survival rate is significantly smaller than the rates from the present study.

The reason why animals with MI acquired such good survival is not fully understood. However, it was clearly observed that the ligation of the peripheral coronary artery before the gradual occlusion of the main trunk of the LAD apparently inhibited the fibrillation during the operation. This procedure is obviously effective at protecting against

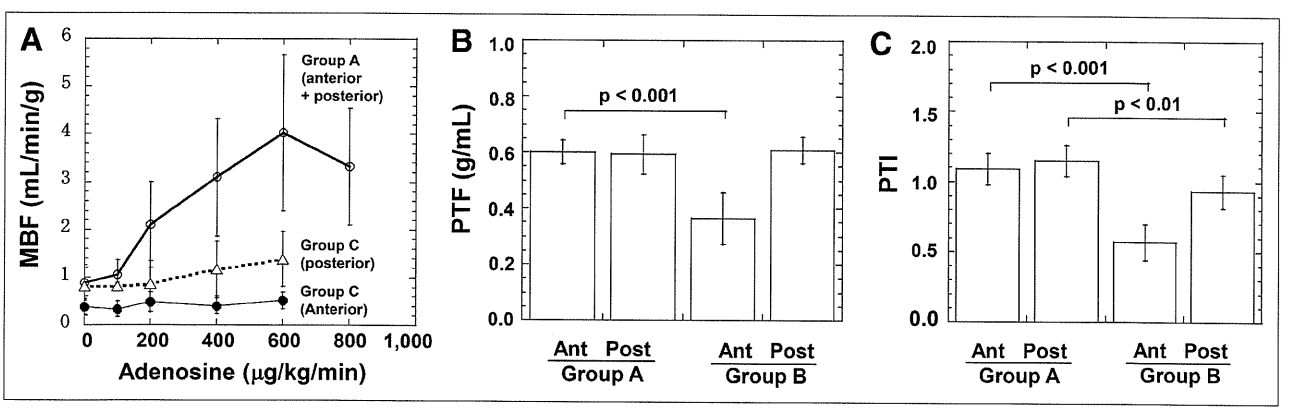

FIGURE 6. Results from PET studies. (A) Regional MBF as function of adenosine dose. In group A, MBF increases with increasing adenosine dose. In infarcted anterior wall of group B, MBF is reduced at rest and does not respond to adenosine. In posterior wall region, adenosine reactivity was significantly reduced. (B and C) Comparison of water-PTF (B) and water-PTI (C). Both were reduced in anterior wall of group B. PTI was also reduced in posterior wall in group B. Ant = anterior; Post = posterior.

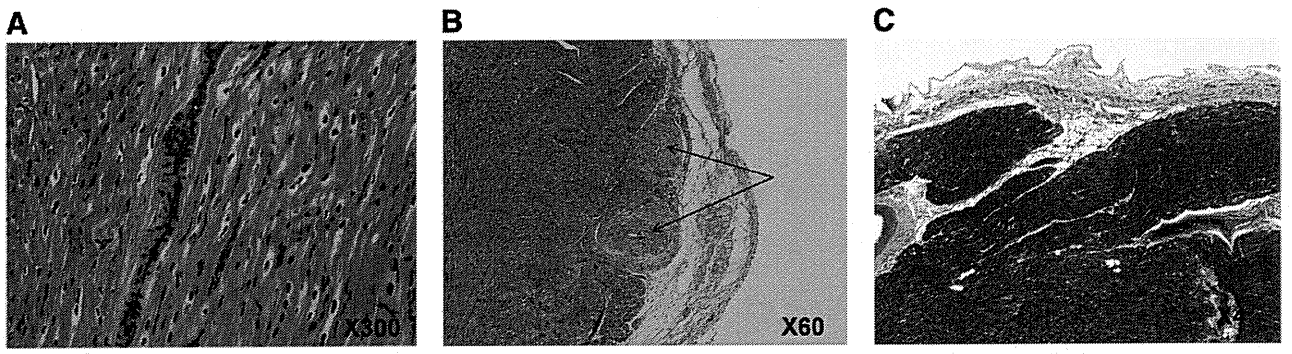

FIGURE 7. Typical images of histologic staining obtained from group B. Hypertrophy with multinuclear muscle cell breeding (A), hyperplasia of blood vessels shown as arrows (B), and denaturation necrosis often seen in subendocardial regions, as in this picture (C), are typical findings.

fatal arrhythmias. This preconditioning effect is supported by the experiments of Moses et al. (*27*), in which ischemic preconditioning of the distal coronary artery protected cardiac muscle through a mechanism involving the potassium channels of mitochondria and myocytes. There may be contributions from other preconditioning factors (*9,28–30*) that associate with increased tolerance of ischemia. Another mechanism could be associated with the modulation of sympathetic tone. It has been reported that regional heterogeneity in myocardial cellular mechanisms (responsible for myocardial cellular depolarization) and repolarization in hibernating myocardium (*12*) can induce ventricular fibrillation (*9*). Inhibition of such heterogeneous myocardial cellular mechanisms or control of modulated sympathetic tone could be another possible explanation.

The present study used a gradual total occlusion of the proximal of LAD, as evidenced by the coronary angiography (Fig. 4), and thus caused an MI of approximately 27% of the total myocardium. The global LV ejection fraction in group B was significantly reduced (39% vs. 66% in controls), showing that LV systolic function was impaired in group B. Both histology and PET had concordant findings. The baseline MBF in the MI area was reduced and was not responding to adenosine administration. This finding is reasonable because the infarcted tissue should have reduced capillary density, and the resistive vessels do not respond to any vasodilating stimulation. The physical extent and size of the MI were reproducible among the individual animals. This feature is important when this animal model is applied to evaluate various new pharmaceuticals or various regenerative therapeutic trials.

The noninfarcted myocardium developed clear signs of remodeling, such as hypokinesis, hypertrophy, and the accumulation of fibrotic tissue in the remote myocardial wall, and significantly decreased PTI values, a marker of residual fractionation of water-perfusable tissue. The baseline MBF was preserved, but reactivity to the adenosine was blunted, even at a maximum dose of 600 μg/kg/min. This reduced reactivity could be related to the degeneration of small arteries, possibly caused by enlargement of myocytes and development of moderate denaturation necrosis and fibrosis.

This study demonstrated that physiologic status and physical extent of MI can be evaluated using the noninvasive technique of PET. The defect surface area identified with ^{18}F-FDG was identical to that identified with PTF, and both agreed well with the results of histology. Furthermore, microscopic degeneration can be characterized as reduced reactivity of quantitative myocardial perfusion to adenosine. The PET-derived PTI, which is known to indicate the absolute fraction of non–scar tissue within the area (*22*), was reduced not only in the infarcted anterior wall but also in the remote region by 10%. As demonstrated in recent studies (*31–34*), the reduced PTI in a control region is thought to be caused by the development of microscopic fibrosis.

In this study, left-atrial and LV pressure analyses have not been measured, because the aims of this study were to create a long-survival pig model of MI and global LV dysfunction with remodeling, characterize this model using PET, and compare these parameters with histology before making a complete model of CHF after MI in pigs. One limitation of this study was that, because of technical reasons in our laboratory at the initiation of this study, it was difficult to measure left-atrial and LV pressures.

CONCLUSION

Our pig model of postinfarction global LV dysfunction was characterized by a high survival rate and large MI, with clear signs of cardiac remodeling, as demonstrated by PET and histology. This animal model might contribute to investigations of MI and new therapies for cardiac remodeling in MI.

ACKNOWLEDGMENTS

We thank the staff of the Department of Investigative Radiology of National Cardiovascular Center for invaluable technical assistance. This study was supported by a re-

search grant from New Energy and Industrial Technology Development Organization (NEDO), Japan, and grants for translational research and nanomedicine from the Ministry of Health, Labor and Welfare (MHLW), Japan.

REFERENCES

1. Saito I, Folsom AR, Aono H, Ozawa H, Ikebe T, Yamashita T. Comparison of fatal coronary heart disease occurrence based on population surveys in Japan and the USA. *Int J Epidemiol.* 2000;29:837–844.
2. Balady GJ, Jette D, Scheer J, Downing J. Changes in exercise capacity following cardiac rehabilitation in patients stratified according to age and gender: results of the Massachusetts Association of Cardiovascular and Pulmonary Rehabilitation Multicenter Database. *J Cardiopulm Rehabil.* 1996;16:38–46.
3. Krum H, Haas SJ, Eichhorn E, et al. Prognostic benefit of beta-blockers in patients not receiving ACE-inhibitors. *Eur Heart J.* 2005;26:2154–2158.
4. Anversa P, Leri A, Kajstura J. Cardiac regeneration. *J Am Coll Cardiol.* 2006;47:1769–1776.
5. Gheeraert PJ, Henriques JP, De Buyzere ML, De Pauw M, Taeymans Y, Zijlstra F. Preinfarction angina protects against out-of-hospital ventricular fibrillation in patients with acute occlusion of the left coronary artery. *J Am Coll Cardiol.* 2001;38:1369–1374.
6. Millard RW. Induction of functional coronary collaterals in the swine heart. *Basic Res Cardiol.* 1981;76:468–473.
7. Roth DM, Maruoka Y, Rogers J, White FC, Longhurst JC, Bloor CM. Development of coronary collateral circulation in left circumflex Ameroid-occluded swine myocardium. *Am J Physiol.* 1987;253:H1279–H1288.
8. Fallavollita JA, Riegel BJ, Suzuki G, Valeti U, Canty JM Jr. Mechanism of sudden cardiac death in pigs with viable chronically dysfunctional myocardium and ischemic cardiomyopathy. *Am J Physiol Heart Circ Physiol.* 2005;289:H2688–H2696.
9. Canty JM Jr, Suzuki G, Banas MD, Verheyen F, Borgers M, Fallavollita JA. Hibernating myocardium: chronically adapted to ischemia but vulnerable to sudden death. *Circ Res.* 2004;94:1142–1149.
10. Fallavollita JA, Canty JM Jr. Differential ^{18}F-2-deoxyglucose uptake in viable dysfunctional myocardium with normal resting perfusion: evidence for chronic stunning in pigs. *Circulation.* 1999;99:2798–2805.
11. Fallavollita JA, Canty JM Jr. Ischemic cardiomyopathy in pigs with two-vessel occlusion and viable, chronically dysfunctional myocardium. *Am J Physiol Heart Circ Physiol.* 2002;282:H1370–H1379.
12. Fallavollita JA, Logue M, Canty JM Jr. Stability of hibernating myocardium in pigs with a chronic left anterior descending coronary artery stenosis: absence of progressive fibrosis in the setting of stable reductions in flow, function and coronary flow reserve. *J Am Coll Cardiol.* 2001;37:1989–1995.
13. Shen YT, Vatner SF. Mechanism of impaired myocardial function during progressive coronary stenosis in conscious pigs: hibernation versus stunning? *Circ Res.* 1995;76:479–488.
14. Mills I, Fallon JT, Wrenn D, et al. Adaptive responses of coronary circulation and myocardium to chronic reduction in perfusion pressure and flow. *Am J Physiol.* 1994;266:H447–H457.
15. Roth DM, White FC, Nichols ML, Dobbs SL, Longhurst JC, Bloor CM. Effect of long-term exercise on regional myocardial function and coronary collateral development after gradual coronary artery occlusion in pigs. *Circulation.* 1990;82:1778–1789.
16. Shen YT, Lynch JJ, Shannon RP, Wiedmann RT. A novel heart failure model induced by sequential coronary artery occlusions and tachycardiac stress in awake pigs. *Am J Physiol.* 1999;277:H388–H398.
17. *Guide for the Care and Use of Laboratory Animals.* Washington, DC: National Academy Press; 1996.
18. O'Konski MS, White FC, Longhurst J, Roth D, Bloor CM. Ameroid constriction of the proximal left circumflex coronary artery in swine: a model of limited coronary collateral circulation. *Am J Cardiovasc Pathol.* 1987;1:69–77.
19. Iida H, Takahashi A, Tamura Y, Ono Y, Lammertsma AA. Myocardial blood flow: comparison of oxygen-15-water bolus injection, slow infusion and oxygen-15-carbon dioxide slow inhalation. *J Nucl Med.* 1995;36:78–85.
20. DeFronzo RA, Tobin JD, Andres R. Glucose clamp technique: a method for quantifying insulin secretion and resistance. *Am J Physiol.* 1979;237:E214–E223.
21. Knuuti MJ, Nuutila P, Ruotsalainen U, et al. Euglycemic hyperinsulinemic clamp and oral glucose load in stimulating myocardial glucose utilization during positron emission tomography. *J Nucl Med.* 1992;33:1255–1262.
22. Iida H, Tamura Y, Kitamura K, Bloomfield PM, Eberl S, Ono Y. Histochemical correlates of ^{15}O-water-perfusable tissue fraction in experimental canine studies of old myocardial infarction. *J Nucl Med.* 2000;41:1737–1745.
23. Iida H, Rhodes CG, de Silva R, et al. Myocardial tissue fraction: correction for partial volume effects and measure of tissue viability. *J Nucl Med.* 1991;32:2169–2175.
24. Iida H, Rhodes CG, de Silva R, et al. Use of the left ventricular time-activity curve as a noninvasive input function in dynamic oxygen-15-water positron emission tomography. *J Nucl Med.* 1992;33:1669–1677.
25. de Silva R, Yamamoto Y, Rhodes CG, et al. Preoperative prediction of the outcome of coronary revascularization using positron emission tomography. *Circulation.* 1992;86:1738–1742.
26. Yamamoto Y, de Silva R, Rhodes CG, et al. A new strategy for the assessment of viable myocardium and regional myocardial blood flow using ^{15}O-water and dynamic positron emission tomography. *Circulation.* 1992;86:167–178.
27. Moses MA, Addison PD, Neligan PC, et al. Inducing late phase of infarct protection in skeletal muscle by remote preconditioning: efficacy and mechanism. *Am J Physiol Regul Integr Comp Physiol.* 2005;289:R1609–R1617.
28. Kitakaze M, Node K, Minamino T, et al. Role of activation of protein kinase C in the infarct size-limiting effect of ischemic preconditioning through activation of ecto-5′-nucleotidase. *Circulation.* 1996;93:781–791.
29. Kharbanda RK, Mortensen UM, White PA, et al. Transient limb ischemia induces remote ischemic preconditioning in vivo. *Circulation.* 2002;106:2881–2883.
30. Chen PS, Chen LS, Cao JM, Sharifi B, Karagueuzian HS, Fishbein MC. Sympathetic nerve sprouting, electrical remodeling and the mechanisms of sudden cardiac death. *Cardiovasc Res.* 2001;50:409–416.
31. Knaapen P, Boellaard R, Gotte MJ, et al. Perfusable tissue index as a potential marker of fibrosis in patients with idiopathic dilated cardiomyopathy. *J Nucl Med.* 2004;45:1299–1304.
32. Knaapen P, Boellaard R, Gotte MJ, et al. The perfusable tissue index: a marker of myocardial viability. *J Nucl Cardiol.* 2003;10:684–691.
33. Knaapen P, Bondarenko O, Beek AM, et al. Impact of scar on water-perfusable tissue index in chronic ischemic heart disease: evaluation with PET and contrast-enhanced MRI. *Mol Imaging Biol.* 2006;8:245–251.
34. Knaapen P, van Dockum WG, Bondarenko O, et al. Delayed contrast enhancement and perfusable tissue index in hypertrophic cardiomyopathy: comparison between cardiac MRI and PET. *J Nucl Med.* 2005;46:923–929.

TISSUE ENGINEERING: Part A
Volume 17, Numbers 15 and 16, 2011

DOI: 10.1089/ten.tea.2010.0482

Long-Term *In Vivo* Magnetic Resonance Imaging Tracking of Endothelial Progenitor Cells Transplanted in Rat Ischemic Limbs and Their Angiogenic Potential

Carlos A. Agudelo, Ph.D.,[1] Yoichi Tachibana, Ph.D.,[1] Teramoto Noboru, B.Sc.,[2] Hidehiro Iida, Ph.D.,[2] and Tetsuji Yamaoka, Ph.D.[1,3]

Stem cell therapy has been used to repair ischemic tissues in the limbs, in myocardial infarctions, and in the brain. To understand the mechanisms of healing, a contrast agent capable of inducing sufficient magnetic resonance (MR) contrast would be useful in providing fundamental information about the cell migration and incorporation into the ischemic tissue. A magnetic resonance imaging contrast agent composed of dextran and gadolinium chelate was synthesized. Hydroxyl groups of dextran were activated with 1,1′-carbonylbis-1H-imidazole and reacted with propanediamine to obtain aminated dextran. This modified polymer was then reacted with mono-N-succinimidyl 1,4,7,10-tetraazacyclododecane-1,4,7,10-tetraacetate, then with fluorescein isothiocyanate, and finally reacted with gadolinium chloride solution (Dex-DOTA-$Gd3^+$). Endothelial progenitor cells (EPCs) were selected as a stem cell model for magnetic resonance imaging tracking. Cells were isolated from the bone marrow harvested from the femurs and tibias of rats. Dex-DOTA-$Gd3^+$ was then introduced into the EPCs by electroporation. The intracellular stability and cytotoxicity of Dex-DOTA-$Gd3^+$ were evaluated *in vitro*. Dex-DOTA-$Gd3^+$-labeled EPCs were transplanted into a rat model of ischemic limb, and MR images were acquired. Dex-DOTA-$Gd3^+$ was found to efficiently label EPCs over a long duration without significant cytotoxicity. This provides an MR signal sufficient for tracking the EPCs intramuscularly injected into the limb.

Introduction

RECENT PROGRESS IN STEM CELL isolation from different sources such as blood, bone marrow (BM), and adipose tissue, coupled with better understanding of their functions, has led to the development of new applications of stem cell transplantation therapies in areas such as cardiac regeneration,[1,2] hind limb ischemia,[3–5] and stroke.[6] When implanting stem cells in ischemic tissues, the cells will likely differentiate into functional cells or release growth factors that act in a paracrine manner.[7–9] A system for tracking the stem cells *in vivo* would provide insights into many basic and practical questions related to stem cell therapy, such as the mechanisms involved in migration, recruitment, mobilization, and incorporation of cells into tissue.[7] Magnetic resonance imaging (MRI) is a noninvasive method that has the potential to reach the levels of sensitivity and resolution, which are necessary for detection of small quantities of cells and to determine their locations within ischemic tissues.

MRI tracking of cells labeled with iron oxide-based magnetic contrast agents has been used for visualization of many aspects of angiogenesis in different cell types such as the hematopoietic and neural progenitor cells.[10–12] One of the advantages of labeling cells with superparamagnetic iron oxide particles (SPIO) is the high sensitivity obtained compared with that obtained with other contrast agents.[13] Wilhelm *et al.* reported that SPIO-labeled cells can be detected in small quantities (30–60 cells in agarose gel) by high-resolution MRI.[14] Other studies reported stem cell homing to the organs and the BM,[15] differentiation and migration of oligodendrocyte progenitors into brain parenchyma, migration and incorporation of labeled cells to the sites of tumor angiogenesis,[16] and magnetic guiding of the endothelial progenitor cells (EPCs) to a target site.[14] However, despite the great advantages provided by SPIO labeling, some studies have reported certain disadvantages. Magnetic resonance (MR) signals in iron oxide-labeled cells transplanted into a mouse hind limb did not show significant differences from the day 1 to 28 post-transplantation; however, there is evidence for a progressive decrease in the cell number when monitored using genetically introduced bioluminescent signals.

Histological analysis confirmed that macrophages loaded with iron oxide particles were located between muscle

[1]Department of Biomedical Engineering, and [2]Department of Investigative Radiology Advanced Medical Engineering Center, National Cerebral and Cardiovascular Center Research Institute, Suita, Osaka, Japan.
[3]Japanese Science and Technology Agency–Core Research of Evolutional Science and Technology, Chiyoda-Ku, Tokyo, Japan.

bundles but no transplanted cells were detected near the macrophages.[15] Therefore, one of the problems when labeling with iron oxide is the instability to remain in the cells *in vivo*, which can probably be termed as leakage. It is possible that the free SPIO are subjected to endocytosis by macrophages. A similar situation was described in iron oxide-labeled mesenchymal stem cells that were transplanted into a rat model of infarcted myocardium.[16] In addition, iron oxide induces negative contrast in MRI, which, in some cases, can be difficult to attribute to the signal loss of the labeled cells, because of many other sources of negative contrast of MRI in the body.

Our group recently reported the development of a polymeric MRI contrast agent based on a gadolinium-chelated poly(vinyl alcohol).[17] In this study, NIH-3T3 cells were labeled with the contrast agent via electroporation. Cell viability and proliferation were not affected by polymer labeling, and MR measurements showed that labeled cells could be clearly tracked *in vivo*. In this study, we selected EPCs as a stem cell tracking model. The EPCs isolated from the peripheral blood and BM have been used in the therapeutic angiogenesis of ischemic limbs, in stroke, and in myocardial infarction.[18–25]

Advances in the techniques for visualizing EPCs, which are activated by cytokines at the site of injury, are imperative for understanding the mechanisms of proliferation, recruitment, mobilization, and incorporation of EPCs into the foci of vasculogenesis. Although the detection sensitivity of gadolinium chelates is generally lower than that of iron oxide, their positive contrast is easy to detect in a determinant tissue.[26,27] Therefore, we synthesized a water-soluble gadolinium chelate as an alternative MRI contrast agent. This agent, called Dex-DOTA-Gd^{3+}, was designed for labeling EPCs. Dex-DOTA-Gd^{3+} was delivered into EPCs by electroporation to investigate its feasibility for cellular imaging and its capability for tracking the fate of the cells *in vivo* over long periods. In addition, we defined a procedure for properly visualizing labeled EPCs transplanted into a rat model of ischemic limbs.

Materials and Methods

H-NMR measurements

Proton nuclear magnetic resonance (H-NMR) spectra were recorded using a 300-MHz 7.1-T NMR spectrometer (Gemini 2000/300; Varian Inc.). The concentration of paramagnetic species Gd(III) was measured by inductively coupled plasma atomic emission spectroscopy (Model 7510; Shimadzu Co., Kyoto, Japan).

Synthesis of Dex-DOTA-Gd^{3+}

Amination of dextran (MW, 40 kD) was conducted as follows: dextran (10 mmol sugar unit) was dissolved in 60 mL of anhydrous dimethylsulfoxide followed by addition of 1,1′-carbonylbis-1H-imidazole (7.5 mmol). The reaction was allowed to proceed under a nitrogen atmosphere at room temperature for 4 h. 1,3- propanediamine (75 mmol) was then added to the resulting reaction mixture, which was then stirred overnight at room temperature. The reaction product was subsequently purified by dialysis (Spectra/Pore membrane; MW cut-off = 10 kDa) in distilled water. The remaining solution was lyophilized, and dextran-diamine was obtained. About 1% of the total amino groups were reacted with fluorescein-5-EX, succinimidyl ester (FITC; Invitrogen, Molecular Probes®, Eugene).

^{1}H-NMR (D_2O): δ 4.99 (br,CHO_2), 3.605 (br,CHOH), 3.769 (br,CHOH), 5.2 (br,CHO), 3.253 (br,$C(=O)NHCH_2$), 2.88 (br,CH_2NH_2), 1.792 (br,$CH_2CH_2CH_2$), 3.53 (br,CHOH), 3.922–3.983 (br,$CHCH_2$).

Dextran-diamine was diluted in 60 mL of anhydrous dimethylsulfoxide and reacted with mono-N-succinimidyl 1,4,7,10-tetraazacyclododecane-1,4,7,10-tetraacetate (DOTA, 1 mmol of NH_2 in dextran-diamine: 1.2 mmol of DOTA) under a nitrogen atmosphere at room temperature for 1 day. The reaction mixture was purified in distilled water by using a dialysis membrane (Spectra/Pore membrane; MW cut-off = 10 kDa). The final solution was lyophilized, and dextran-diamine-DOTA was obtained.

^{1}H-NMR (D_2O): δ 5.02 (br,CHO_2), 3.63 (br,CHOH), 3.77 (br,CHOH), 5.2 (br,CHO), 3.3 (br,$C(=O)CH_2N$), 3.51 (br,NCH2C(=O)OH), 3.326 (br,$C(=O)NHCH_2$),br,CH_2CH_2N), 1.91 (br,$CH_2CH_2CH_2$), 3.92 (br,CHOH).

Dextran-diamine-DOTA was diluted in 50 mL of distilled water and treated with 2.2 mole equivalents of gadolinium chloride solution, which was added dropwise with stirring. After the stabilization of the solution with addition of 1 M NaOH to obtain a final pH of 6.6–7.0, the reaction product was stirred for 1 day at room temperature. After this, the reaction mixture was purified in distilled water by using a dialysis membrane (Spectra/Pore membrane; MW cut-off = 10 kDa). The final solution was lyophilized, and dextran-DOTA-Gd^{3+} was obtained (Dex-DOTA-Gd^{3+}).

MRI measurements

T_1-weighted images were obtained in a 1.5-*T* compact MRI system (MRmini; Dainippon Sumitomo Pharma) with a TR of 2000 ms and TE of 9 ms (FOV: 4×8 cm; matrix: 126×256; slice thickness: 1 mm; slice gap: 0 mm; number of slices: 35).

Isolation of EPCs

BM was flushed from the femurs and tibias of F344 rats (4-week-old males) after previous cytokine induced mobilization of BM-derived EPCs by subcutaneous injections of granulocyte colony-stimulating factor (Kirin Pharma) at 200 μg/kg/day over 5 days.[28,29] CD34 and FLK-1 positive BM cells were isolated by magnetic beads (Streptavidin Microbeads; Miltenyi Biotec GmbH) coated with the antibodies CD34 and FLK-1 (sc-6251 and sc-7324; Santa Cruz Biotechnology, Inc.) and by using the biotin labeling kit NH_2 (Dojindo Molecular Technologies, Inc.). Cells were placed in fibronectin-coated dishes and cultured with an endothelial cell basal medium (EBM-2) supplemented with EGM-2 SingleQuots (Clonetics Lonza).[18]

Histological identification of EPCs

One week after isolation, the cells were detached using ReagentPack™ (Clonetics Lonza), and 1×10^5 cells were placed in fibronectin-coated dishes (3.5-mm glass bottom dish; Matsunami Glass IND., Ltd.). Fluorescent staining of adherent cells was used to confirm the EPC phenotype. EPCs were incubated with 1,1′-dioctadecyl-3,3,3′,3′-tetramethylindocarbocyanine perchlorate-labeled acetylated LDL (DiI-acLDL,

10 μg/mL; Biomedical Technologies; $n=3$) at 37°C for 4 h.[19,21,24] EPCs were further stained with fluorescein *Griffonia simplicifolia* lectin I, isolectin B4 (10 μg/mL; Vector Laboratories, Inc.; $n=3$) for 2 h.[30,31] Additional staining with endothelial nitric oxide synthase was performed (eNOS; Santa Cruz Biotechnology, Inc.; $n=3$).[31] After staining, the samples were viewed with a confocal microscope (Nikon Eclipse TE 2000-E; Nikon Corporation). Cells with positive fluorescence were identified as EPCs.[19,21,30,31] Six days after implantation of double-labeled EPCs by using Dex-DOTA-Gd^{3+} and a Qtracker® cell 655 labeling kit (Molecular Probes; Invitrogen Detection Technologies, Eugene; labeling was performed according to the manufacturer's instructions), a rat was sacrificed to demonstrate that the MR images of the contrast agent Dex-DOTA-Gd^{3+} when inside the cells actually correspond to the EPCs transplanted into the ischemic limb. Adductor muscle was dissected and subsequently embedded in Tissue-Tek for freezing (Sakura Finetechenical Co. Ltd.). Samples were then observed with a confocal microscope (Nikon Eclipse TE 2000-E; Nikon Corporation) ($n=20$; thickness, 8 μm). Paraffin sections of the excised tissue were then stained for macrophages as follows: Frozen sections were thawed, and the tissue was fixed in acetone. Sections were then washed in TBS buffer (50 mM Tris-HCl buffer containing 0.01% Tween-20 and 0.15 M NaCl) and treated with 0.6% H_2O_2 in 80% methanol at room temperature for 20 min. After washing in TBS buffer, the samples were incubated with mouse antirat CD68 (AbD Serotec) as a primary antibody at 4°C overnight. Sections were washed in TBST and stained with Histofine® Simple Stain MAX PO (Nichirei Biosciences, Inc.) and a second antibody at room temperature for 30 min. After washing in TBST, the tissue was incubated in 3,3'-diaminobenzidine tetrahydrochloride solution until a brown reaction product appeared.

Determination of capillary density

To quantify the effect of transplanted-labeled cells on neovascularization, an assessment was performed by measuring the number of capillaries highlighted by alkaline phosphatase (AP) staining within 36 randomly chosen fields under a light microscope (Nikon Coolscope II, Nikon corporation) in sections taken from the ischemic hind limb (12 measurements/rat) at day 35. Tissue specimens were taken from the adductor and semi-membranous muscles. Capillary density was compared with the nonischemic limb. Frozen sections of tissue (8 μm) were stained with AP substrate kit III (Vector laboratories, Inc.) to detect capillary endothelial cells.[32,33] Additional sections were stained for von Willebrand factor (polyclonal rabbit antihuman) (Dako LSAB System-HRP for use on rat specimens; DakoCytomation) to further confirm the phenotype of the endothelial cells.

Cell labeling by electroporation

After isolation, the EPCs were cultured for 2 months (cells were used in the fourth passage for all experiments) in fibronectin-coated dishes and cultured with EBM-2 supplemented with EGM-2 SingleQuots (Clonetics Lonza) at 37°C in 5% CO_2. Afterward, 5×10^5 cells were counted, placed in 60-mm dishes, and cultured for 1 day. Cells were then washed with phosphate-buffered saline solution (PBS; Invitrogen) and cultured in 3 mL of EBM (phenol red-free; Clonetics Lonza) for 30 min. Dex-DOTA-Gd^{3+} was subsequently added to the medium at a concentration of 10 mM, and electrical pulses were applied to the cells by using a CUY-21 electroporator (NEPPA GENE) under the following conditions: field strength: 300 V/cm, number of pulses: 10, and pulse duration: 5 ms. Cells were then cultured for 1 h and washed several times with PBS.

Dex-DOTA-Gd^{3+}-labeled EPCs were divided and placed into fibronectin-coated dishes for further microscopy analysis (35-mm dishes, 27-mm quartz bottom, 1.2×10^5 per dish; $n=30$). To verify whether Dex-DOTA-Gd^{3+} leakage from the cells occurred after electroporation, the cells were washed with PBS and treated with 1 mL of lysis buffer (25 mM Tris; pH 7.8, 2 mM 1,2-diamino-cyclohexane-N,N,N',N'-tetraacetic acid, 10% glycerol, and 1% Triton X-100). After 1 h of incubation at 37°C, 100 μL of the resulting solution was placed in a 96-well plate, and the fluorescence intensity was measured with a fluorometer ($n=10$; excitation: 430 nm, emission: 540 nm; Wallac 1420 ARVO SX; Perkin-Elmer Life Sciences). With the known quantity of Gd in the polymer, the Gd inside the cells could be determined by linear regression analysis of the known fluorescence intensity of the cell lysate versus the fluorescence intensity of the Dex-DOTA-Gd^{3+} at different concentrations.

Cytotoxicity

Cytotoxicity was analyzed by a lactate dehydrogenase cytotoxicity test (Wako Pure Chemical Industries, Ltd.; performed according to the manufacturer's instructions) after coculturing 10^4 EPCs with different concentrations of Dex-DOTA-Gd^{3+} for 24 h. Additionally, the tetrazolium salt (WST-1) was used to measured cell proliferation and viability (Premix WST-1 cell proliferation assay system; Takara BIO Inc.). Dex-DOTA-Gd^{3+}-labeled and nonlabeled EPCs were placed in 12-well plate fibronectin-coated dishes (4×10^4 cells/well). The Premix WST-1 ready-to-use solution was added to the wells (100 μL solution/mL of medium), and the cells were incubated at 37°C under 5% CO_2 for 24 h. The absorbance was measured, and the cell quantity was calculated using a linear regression analysis of the fluorescence intensity of nonlabeled EPC in a determined number. Samples were collected thrice per week over a period of 10 days ($n=6$).

Relaxivity

T_1 relaxation was estimated for each gadolinium complex. Longitudinal relaxation times (T_1) were measured by a combination of measurements made in a large NMR tube (650 μL of distilled water to dilute the polymer to different concentrations) and in a small tube (containing 50 μL of benzene-D6). An attenuator was used to obtain the signal of water protons. Samples were measured in a 300-MHz (7.1-T) NMR spectrometer (Gemini 2000/300; Varian Inc.) by using an inversion recovery technique with 19 inversion times, ranging from 1 to 5000 ms at room temperature (25°C). A typical 180° pulse was for 19 μs. T_1 values were calculated by a least-square fitting analysis of the signal intensities measured at 19 inversion times values in an exponential fashion. The relaxivity of the gadolinium complex was determined by a linear regression of $1/T_1$ versus the concentration of the gadolinium complex.

Rat ischemic limb model

Male F344 rats (8-week-old) were anesthetized with isoflurane (1.5% in the air). The left femoral artery and vein and their branches were ligated and excised completely through a skin incision. The femoral artery and vein were excised from their proximal origin as a branch of the external iliac artery to the distal point where it bifurcates into the saphenous and popliteal arteries.[34] Rats ($n=8$) were injected in 3 places with a total of 150 μL of Bolheal® containing Dex-DOTA-Gd^{+3}-labeled EPCs inside the muscle at the inguinal region where the femoral artery and vein were excised. Injections were applied as follows: To allow normal movement of the cell through the muscle, 6.3×10^6 labeled cells in 50 μL of Bolheal component A (thrombin, 250 units/mL) were intramuscularly injected in three different places in the abductor and quadriceps (total, $1.8–2.0\times10^7$ cells), and 50 μL of Bolheal component B (fibrinogen, 80 mg/mL) was then injected at the same sites to temporarily immobilize the cells (gelation occurred in the muscle). Ischemic limb controls ($n=8$) were injected with 150 μL of Bolheal without cells.

Statistical analysis

All data are expressed as means ± SD. Statistical significance was evaluated using an unpaired two-tailed Student's *t*-test for two variables. Differences were considered significant when p values were less than 0.05.

Results

MRI contrast agent

To develop a suitable MRI contrast agent for EPCs, we selected dextran (MW = 40 KDa) because of its biocompatibility, rapid clearance in the body,[35] biodegradability,[36] and approval by the U.S. Food and Drug Administration (Fig. 1). Inductively coupled plasma atomic emission spectroscopy revealed that 19.5% of OH groups reacted with DOTA-Gd in the contrast agent structure, which corresponds to $m=48$ and $n=199$.

Figure 2a shows the MR images of Dex-DOTA-Gd^{+3} aqueous solutions at different concentrations. MR contrast agents shorten the longitudinal relaxation time *T*1 value,

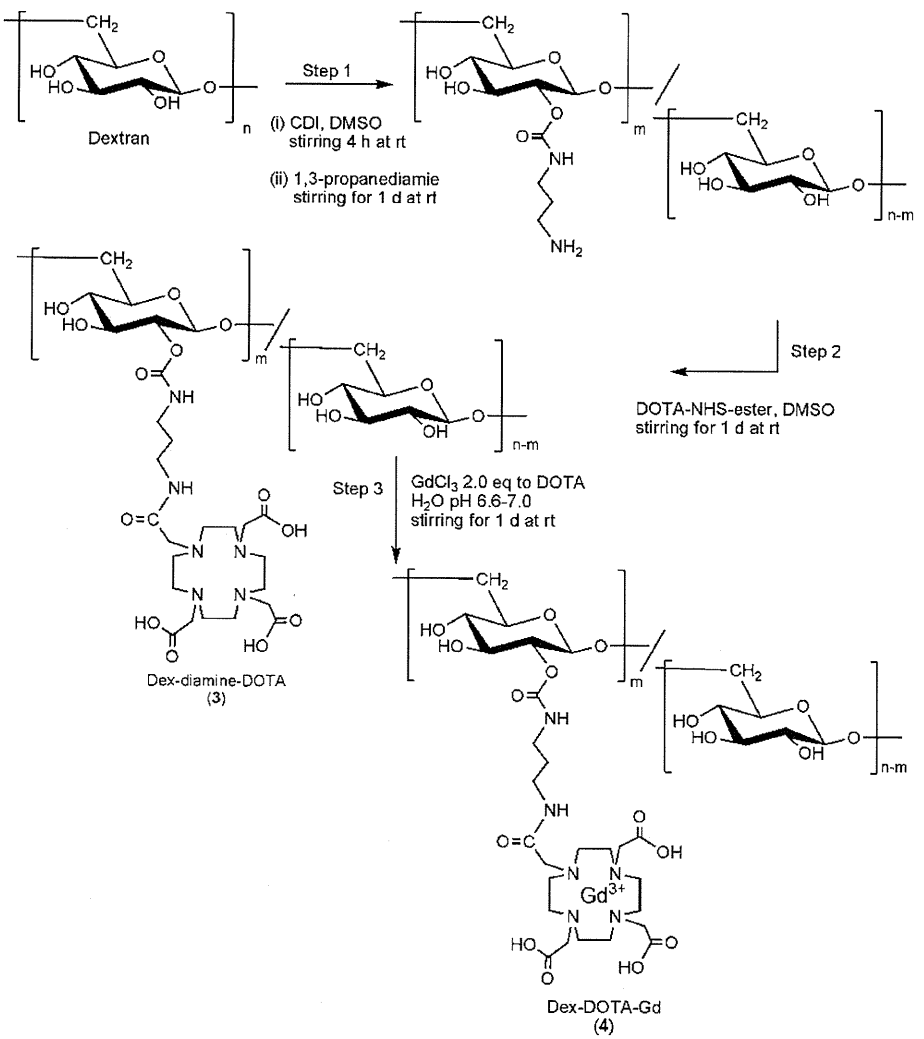

FIG. 1. Synthesis of MRI contrast agent. Schematic structure of Dex-DOTA-Gd^{3+}, which consists of a dextran derivative modified with the gadolinium (III) chelate DOTA-Gd^{3+}. MRI, magnetic resonance imaging.

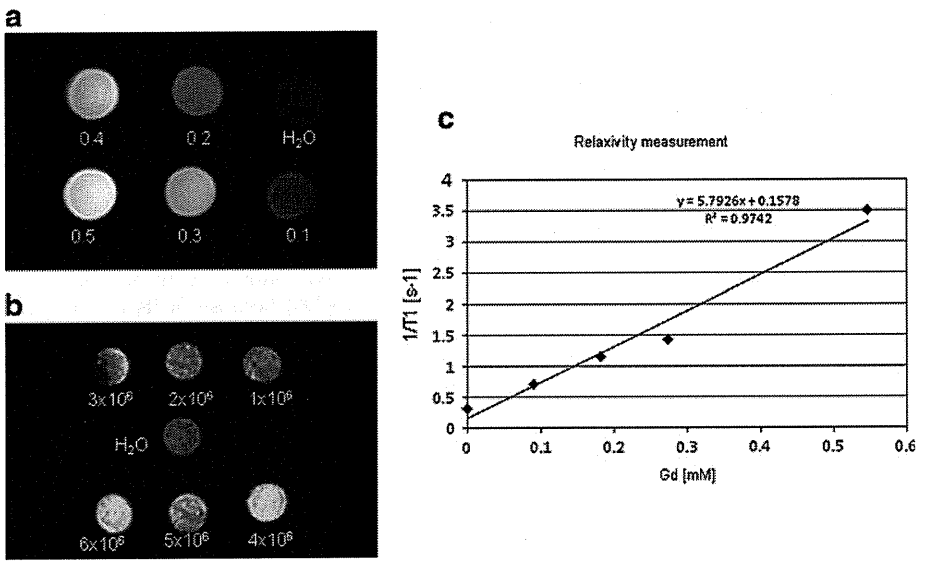

FIG. 2. Properties of the MRI contrast agent **(a)** MR images of Dex-DOTA-Gd^{3+} aqueous solutions. *T*1-weighted images of the samples were acquired with 2D- and 3D-spin echo sequences with a repetition time (TR) of 300, an echo time (TE) of 12 ms, and an image acquisition matrix of 128×256. Fifty microliters of Dex-DOTA-Gd^{3+} solutions containing 0.1, 0.2, 0.3, 0.4, and 0.5 mmol polymer unit was used. **(b)** MRI images of EPCs containing Dex-DOTA-Gd^{3+} as the contrast agent (10 mM in unit and 19.5 Gd as introduction ratio when labeling) in 100 μL of agarose hydrogel. Sequence: 2D spin echo; coronal slice, 1 mm; TR, 2000 ms; TE, 9 ms; image acquisition matrix, 128×256; and 0.12 pg Gd/cell. **(c)** Relaxivity measurements of Dex-DOTA-Gd^{3+}. *T*1 was measured using a combination of an NMR tube (650 μL of distilled water diluting the polymer to different concentrations) and a small tube containing 50 μL of benzene-D6. An attenuator was used to obtain the signal of water protons. EPCs, endothelial progenitor cells; NMR, nuclear magnetic resonance.

which is defined as the time constant of the exponential recovery of proton spins to their equilibrium along an applied field after disturbance. The relaxivity (*R*1) for Dex-DOTA-Gd^{3+}, which represents the reciprocal of the relaxation time per unit of Gd concentration in s^{-1}/mM, was determined by measuring the longitudinal relaxation time *T*1 values of several aqueous solutions by NMR and plotting 1/*T*1 versus the polymer concentration. Dex-DOTA-Gd^{3+} showed a relaxivity value of 5.8 s^{-1}/mM (Fig. 2c), which, in comparison with approximate values of about 4.2 s^{-1}/mM for DOTA-Gd and 3.8 s^{-1}/mM for gadolinium-diethylenetriaminepentaacetic acid (DTPA-Gd),[37,38] represents an increase of 38% and 52.6% over the relaxation value. Therefore, an enhancement of visualization of the resolution in MR images with Dex-DOTA-Gd^{3+} as a contrast agent is possible in comparison with the standard Gd^{3+} and Magnevits®. MR images of Dex-DOTA-Gd^{3+} aqueous solutions show an increase in signal intensity with regard to an increase in the concentration of the polymer (Fig. 2a). This increase is due to a reduction in the longitudinal relaxation time. Moreover, images show that the Gd complex has the capacity to return to its equilibrium state after radio frequency excitation. It can be seen that Dex-DOTA-Gd^{3+} MR images obtained at a concentration of 0.2 mM are visually different from MR images of distilled water.

Labeling of EPCs

The phenotype of the EPCs was then confirmed by immunostaining with DiI-acLDL, and staining with lectin and eNOS (Fig. 3). All cells were confirmed as the EPC phenotype based on their capacity to incorporate acetylated low-density lipoprotein, to bind lectin, and to bind endothelial nitric oxide synthase throughout the process of obtaining images (Fig. 3).[30,31] Both FLK-1 and CD34 are expressed by all hematopoietic stem cells and EPCs, but cease to be expressed during hematopoietic differentiation.[18,19]

EPC cells were labeled with Dex-DOTA-Gd^{3+} by means of electroporation and placed into agarose hydrogel. Figure 2b shows MR images of EPCs containing Dex-DOTA-Gd^{3+} in 100 μL of agarose hydrogel. The amount of labeled cells necessary to obtain differences in contrast with regard to water was found to be 1×10^6 (1.11×10^{-10} mmol Gd), and the quantity of gadolinium incorporated into each cell was 0.12 pg of Gd. Cytotoxicity was analyzed by a lactate dehydrogenase cytotoxic test. Percentages of viable cells labeled

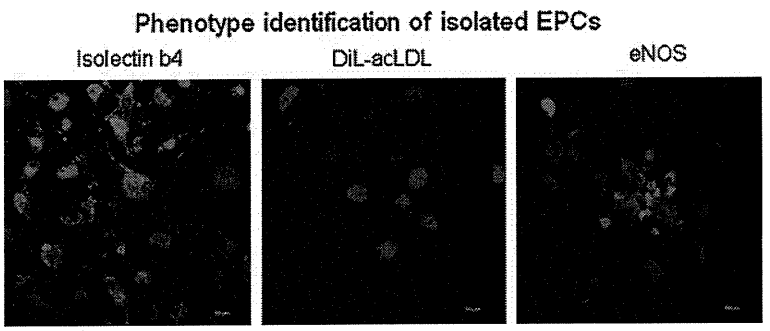

FIG. 3. Phenotype identification of the isolated EPCs. One week after isolation, fluorescent staining of the adherent cells was used to confirm the EPC phenotype. Cells were incubated with DiI-acLDL, isolectin B4, and eNOS. After staining, the samples were visualized with a confocal microscope. The cells demonstrated positive fluorescence, which indicates the EPC phenotype. Scale bar = 50 μm. eNOS, endothelial nitric oxide synthase. Color images available online at www.liebertonline.com/tea

with Dex-DOTA-Gd^{3+} at different concentrations are shown in Figure 4a. This clearly shows that for Dex-DOTA-Gd^{3+} concentrations lower than 15 mM, cell viability is as high as 90%, whereas higher concentrations of Dex-DOTA-Gd^{3+} were found to be slightly toxic, but with a range between 70% and 80% cell viability.

Therefore, we selected a polymer concentration of 10 mM to label the cells, because this concentration has low toxicity while providing an adequate quantity of gadolinium to achieve the required T_1 shortening and high resolution for tracking labeled cells. Consistent with the previous results, the WST-1 assay performed with 10-mM polymer concentration revealed that EPCs were not affected by the contrast agent at least within 10 days after electroporation when cells achieved maximum confluence. No statistical differences were identified between the proliferation of nonlabeled EPCs and Dex-DOTA-Gd^{3+}-labeled EPCs.

To analyze the distribution and stability of the contrast agent inside the cells, the Dex-DOTA-Gd^{3+}-labeled cells were cultured for 25 days. As seen in Figure 4b, the EPCs exhibit a remarkably high degree of intracellular labeling with the cytoplasm containing large amounts of contrast agent. Interestingly, no further transport in the nuclei was observed 25 days after labeling. Figure 4c shows the Dex-DOTA-Gd^{3+} concentration inside cells with regard to the culture period and cellular proliferation rate.

The quantity of polymer remained stable for 25 days after electroporation. This suggests that Dex-DOTA-Gd^{3+} did not leak out of the cells during the culture period, and that the cells grew well. The differences detected from day 1 to 25 were not statistically significant ($p > 0.05$), demonstrating stability of Dex-DOTA-Gd^{3+} labeling.

In vivo *tracking of EPCs*

Having demonstrated successful cellular MR imaging of EPCs by means of Dex-DOTA-Gd^{3+}, we wanted to determine the efficacy of our MRI contrast agent for detecting and tracking EPCs in an *in vivo* rat model of ischemic hind limb. Immediately after inducing ischemia, we injected rats with Dex-DOTA-Gd^{3+}-labeled EPCs in the adductor and quadriceps muscle in the inguinal region where the femoral artery and vein were excised (Bolheal was used to temporarily immobilize cells, as indicated in the Methods section). Animals were imaged thrice per week to determine the fate of the transplanted cells in the tissue. Figure 5 shows MR im-

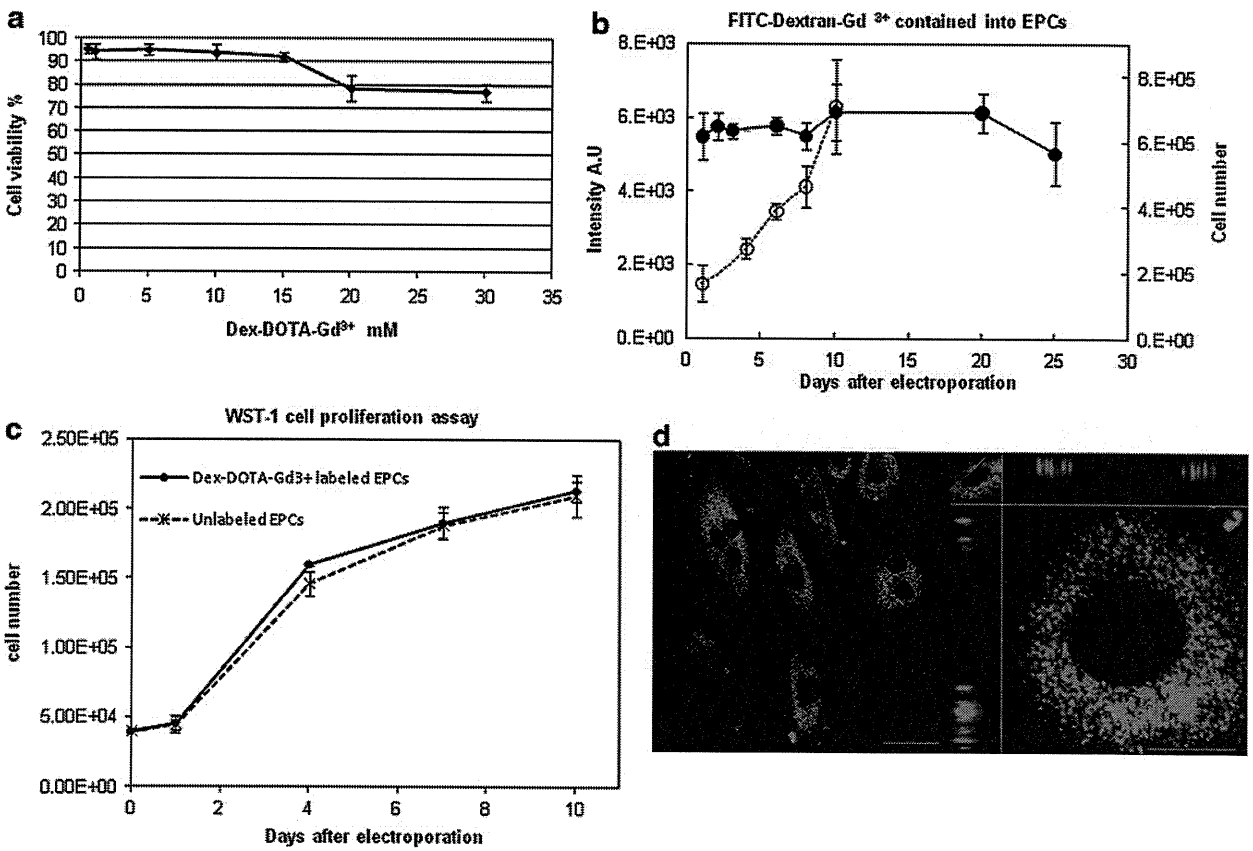

FIG. 4. **(a)** Viability of EPCs as measured by lactate dehydrogenase assay at different Dex-DOTA-Gd^{3+} concentrations. **(b)** Stability of Dex-DOTA-Gd^{3+} in EPCs after electroporation (solid mark) and cell proliferation (open mark). Fluorescence intensity mean (±SD) values are shown; no statistically significant differences were identified on the first day after electroporation ($n = 5$). $p > 0.05$. **(c)** Proliferation activity and viability of EPCs were assessed by WST-1 cell proliferation assay. The cell quantity was measured by its absorbance. The mean (±SD) values of cell number are shown; no statistically significant differences were identified between the labeled and unlabeled EPCs ($n = 6$). $p > 0.05$. **(d)** Confocal microscopy of Dex-DOTA-Gd^{3+}-labeled EPCs after electroporation. Scale bar = 40 μm (left) and 20 μm (right). Color images available online at www.liebertonline.com/tea